LA-UR-18-23470

Draft version December 12, 2021
Typeset using LaTeX **twocolumn** style in AASTeX62

NEW FORMATION MODELS FOR THE KEPLER-36 SYSTEM

Peter Bodenheimer,[1] David J. Stevenson,[2] Jack J. Lissauer,[3] and Gennaro D'Angelo[4]

[1] *UCO/Lick Observatory, Department of Astronomy and Astrophysics, University of California, Santa Cruz, CA 95064, USA*
[2] *Division of Geological and Planetary Sciences, Caltech, Pasadena, CA 91125, USA*
[3] *Space Science and Astrobiology Division, NASA-Ames Research Center, Moffett Field, CA 94035, USA*
[4] *Theoretical Division, Los Alamos National Laboratory, Los Alamos, NM 87545, USA*

(Received June, 28; Revised October, 8; Accepted October, 15; To appear in The Astrophysical Journal)

ABSTRACT

Formation of the planets in the Kepler-36 system is modeled by detailed numerical simulations according to the core-nucleated accretion scenario. The standard model is updated to include the dissolution of accreting rocky planetesimals in the gaseous envelope of the planet, leading to substantial enrichment of the envelope mass in heavy elements and a non-uniform composition with depth. For Kepler-36 c, models involving in situ formation and models involving orbital migration are considered. The results are compared with standard formation models. The calculations include the formation (accretion) phase, as well as the subsequent cooling phase, up to the age of Kepler-36 (7 Gyr). During the latter phase, mass loss induced by stellar XUV radiation is included. In all cases, the results fit the measured mass, 7.84 $M_\oplus$, and radius, 3.68 $R_\oplus$, of Kepler-36 c. Two parameters are varied to obtain these fits: the disk solid surface density at the formation location, and the "efficiency" factor in the XUV mass loss rate. The updated models are hotter and therefore less dense in the silicate portion of the planet and in the overlying layers of H/He, as compared with standard models. The lower densities mean that only about half as much H/He is needed to be accreted to fit the present-day mass and radius constraints. For Kepler-36 b, an updated in situ calculation shows that the entire H/He envelope is lost, early in the cooling phase, in agreement with observation.

Keywords: planets and satellites: formation — planets and satellites: physical evolution — planets and satellites: individual (Kepler-36 c, Kepler-36 b)

1. INTRODUCTION

Thousands of extrasolar planets have been discovered during the past decade. A substantial fraction of these were found through transit observations by the main *Kepler* mission, which identified more than 4000 planetary candidates, the majority of which have been verified as true exoplanets (https://www.nasa.gov/kepler/discoveries). The general observed properties of extrasolar planets are reviewed by Winn & Fabrycky (2015) and Lissauer et al. (2014). Most of the *Kepler* planets orbit within 0.5 AU of their star, and have radii between those of Earth and Neptune. A subset of the *Kepler* planets also have mass determinations, as found either by radial velocity measurements of the transiting planets (Marcy et al. 2014), or by transit timing measurements in systems with multiple planets (Agol & Fabrycky 2018). A diagram of the radii and masses of such objects, with radii $R < 4.2$ $R_\oplus$, can be found in Kaltenegger (2017). For example, transit timing variations in the Kepler-11 system yield masses between 1.9 and 8.0 $M_\oplus$ for planets with radii between 1.8 and 4.2 $R_\oplus$ (Lissauer et al. 2013).

We consider planets in the range 1–10 $M_\oplus$ and radii $R < 6$ $R_\oplus$. The mass and radius measurements give the planetary mean density $\bar{\rho}$. Those with $\bar{\rho} > 5.0$ g cm^{-3} $(M_p/M_\oplus)^{0.7}$ must be composed almost entirely of heavy elements (primarily rock) with hardly any hydrogen/helium (H/He) atmosphere. This conclusion is true for planets of $R = 1$ $R_\oplus$, but larger planets must be more dense for heavy elements to dominate by volume. The low-density planets ($\bar{\rho} < 1.5$ g cm^{-3}) can

peter@ucolick.org
djs@gps.caltech.edu
Jack.J.Lissauer@nasa.gov
gennaro@lanl.gov

still have most of their mass in a heavy-element core of rock and (possibly) ice, but they must also have a volumetrically significant outer envelope occupied by light gasses (H and/or He). Intermediate-density planets can resemble the low-density planets but with the outer envelope occupying a smaller fraction of the volume, or they could be composed mostly of water and/or other astrophysical ices. Observationally there appears to be a boundary in radius between those planets that are composed (almost) entirely of heavy elements and those with a light-element envelope. Based on a limited sample of transiting planets with radial-velocity mass determinations, Rogers (2015) finds that few planets larger than 1.6 $R_\oplus$ are composed entirely of rock (silicates plus iron). Above 2 $R_\oplus$, the planet is very likely to have a substantial fraction of its volume occupied by light elements. Further observations indicate a bimodal distribution of planetary radii (Fulton & Petigura 2018; Van Eylen et al. 2018), with a definite dip in the number of planets with radii around 1.8 $R_\oplus$. Most planets with orbital periods less than 100 days have radii either < 1.6 $R_\oplus$ or 2–3 $R_\oplus$.

A particularly interesting system in this regard is that of the star Kepler-36 (Carter et al. 2012), an evolved subgiant with mass 1.07 $M_\odot$ and radius 1.626 $R_\odot$. The planet Kepler-36 b has an orbital period of 13.84 days, a mass of 4.32 (+0.19, −0.20) $M_\oplus$, and a radius of 1.49 ± 0.035 $R_\oplus$, while its neighbor Kepler-36 c has a period of 16.238 days, a mass of 7.84 (+0.33, −0.36) $M_\oplus$, and a radius of 3.68 (+0.056, −0.055) $R_\oplus$ (Deck et al. 2012). The masses are determined from transit timing variations and refined by considerations of long-term orbital stability of the system (Deck et al. 2012). The precision of the masses and radii of the two planets is among the best available for extrasolar planets; thus, this system is a prime target for theoretical analysis. Standard structure models (Lopez & Fortney 2013) indicate that planet c is likely to have an H/He envelope containing about 9% of the total mass, while planet b is likely to be a rocky planet with no H/He envelope, or at most one with less than 0.1% of the mass. The mean densities of planets b and c are, respectively, $\approx 7.23 \pm 0.61$ and $\approx 0.87 \pm 0.055$ g cm^{-3}. Mean densities of a number of well-observed planets, including those of Kepler-36, are shown in Figure 1.

Model calculations of the evolution of the Kepler-36 planets, starting after formation at an age of 10 Myr and ending at the present age of the star (6.92 ± 0.37 Gyr) are reported by Lopez & Fortney (2013). The model planets are located on their current orbits. The models consist of a heavy-element core, with constant mass $M_{\rm core}$, equal to the present deduced core masses of the planets, and a H/He envelope, which cools and loses mass with time as a result of XUV irradiation from the star. Both planets are assumed to start with a H/He mass fraction of 22%, and the results show agreement with the current masses and radii of the planets. Planet b loses its entire H/He envelope, while planet c is left with an envelope with mass fraction about 9%. The enhanced mass loss in planet b is not primarily a result of the slightly higher XUV flux (the orbital radii of planets b and c differ by ≈ 10%), but rather because of the significantly lower $M_{\rm core}$, which makes the planet more susceptible to mass loss. These authors show that the mass loss time scale goes roughly as $M_{\rm core}^2$.

Similar calculations were performed by Owen & Morton (2016), again starting after formation and with the orbits at their present positions. Some differences in assumptions were made regarding the XUV mass loss rate and the dependence of the XUV flux on time. The conclusion was that planet b started with an envelope mass fraction of less than about 10% and that the planet lost its entire envelope, while planet c started with an envelope mass fraction of 15–30% and retained an H/He envelope with mass fraction about 10%.

This paper investigates the origin and evolution of the Kepler-36 planets, assuming that they form somewhere in the inner disk, inside the snow line, according to the core-nucleated accretion process (Safronov 1969; Pollack et al. 1996; D'Angelo & Lissauer 2018). In our past work (Pollack et al. 1996; Movshovitz et al. 2010; Rogers et al. 2011; D'Angelo & Bodenheimer 2016) and references therein, the accreting planetesimals orbit through the gaseous envelope, ablating and breaking up during the process. The amount of solid material that is deposited at each layer of the envelope is determined. However, in practically all calculations, the heavy-element material is assumed to sink to the core, leaving the envelope with a composition of pure H/He. A small amount of dust remains in the atmosphere and is a source of opacity to outgoing thermal radiation, but only the overwhelmingly dominant elements H and He are included in the calculations of the equation of state within the envelope. The main improvement in the present work involves the fate of the accreted planetesimals, which are allowed to break up, vaporize, and dissolve in the H/He envelope, thereby enriching the envelope, non-uniformly, in heavy elements.

Several previous calculations have considered this effect. Venturini et al. (2016) assume that a planet forms beyond the ice line and accretes planetesimals composed of rock and ice. All of the rock sinks to the core, and a fraction of the ice (nominally 50%) remains in the envelope while the remainder sinks. The ices in the envelope are uniformly mixed throughout its entire mass, so the envelope composition is uniform at all times, but enriched in ices compared with solar composition. The authors find that various types of planets, including giant planets as well as Neptune-type planets, can be formed through such envelope enrichment. Also, the formation of gas giants is accelerated by this process, and the planetary metallicity is predicted to decrease with increasing planetary mass.

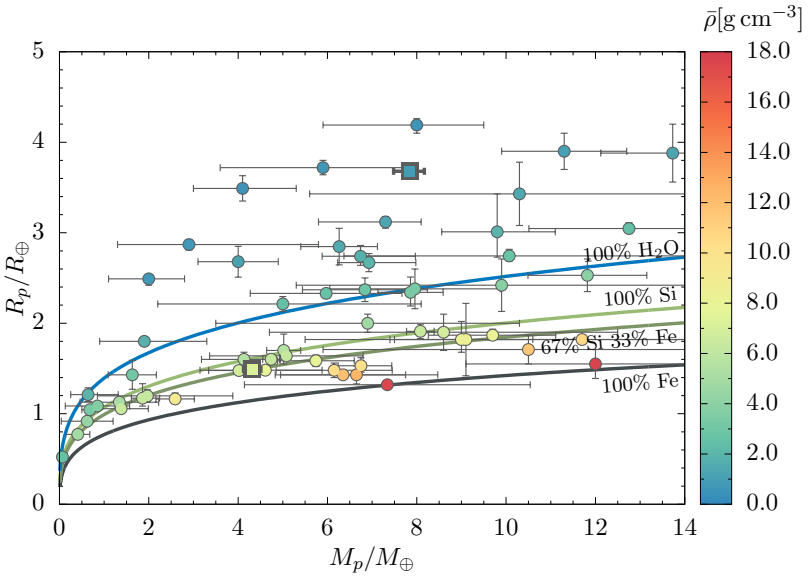

Figure 1. Radius (R_p) versus mass (M_p) of selected extrasolar planets whose mass and radius have both been measured (source: NASA Exoplanet Archive). Some planets with large error bars have not been plotted. The color scale renders the average density, computed from the mass and radius values. The vast majority of the planets were observed by the *Kepler* mission. The four curves indicate the radius of solid cores of different compositions, as indicated (D'Angelo & Bodenheimer 2016). The two squares indicate Kepler-36 b (less massive) and c.

Further calculations are reported by Venturini & Helled (2017); again all of the rock component of the planetesimals sinks to the core, while all of the ice remains uniformly mixed in the envelope. Formation locations range from 5 to 30 AU, with subsequent orbital migration, and planetesimal accretion as well as pebble accretion is considered. The object is to determine the occurrence rate of mini-Neptunes, that is, planets with mass $M_{\rm p} < 10$ M$_\oplus$ and with H/He mass fractions between 0.1 and 0.25. This occurrence rate is found to depend on solid particle size, formation location, and envelope opacity. For low opacity with pebbles, the rate is found to increase when envelope enrichment is included and the formation location is around 20–30 AU. For low opacity with planetesimals, the same is true if the formation location is around 5 AU. For high opacity, for both pebbles and planetesimals, the favored location is at 20–30 AU, and the rate increases significantly with envelope enrichment.

Formation calculations for Jupiter (Lozovsky et al. 2017) include envelope enrichment in heavy elements but are based on pre-computed structure models for the formation of the planet. It is not assumed that the rock portion of the rock/ice planetesimals falls to the core or that uniform mixing necessarily occurs. Early on, planetesimals do accrete to form a solid/liquid core, but once this core reaches 1–2 M$_\oplus$, they dissolve in the envelope, forming a non-uniform composition distribution. Silicate vapor tends to concentrate toward the center, and its presence leads to much higher temperatures in the envelope than those in envelopes composed of pure hydrogen/helium. Most of the accreted heavy-element material remains in the envelope and does not settle to the core. A further calculation for Jupiter, again without the assumption of uniform mixing, investigates the structure allowing for a gradient in the mass fraction of heavy elements (Helled & Stevenson 2017). That gradient could be quite steep, leading to a fairly well-defined core/envelope structure, or it could be quite gradual, depending on the history of the gas accretion rate compared with the solid accretion rate.

Chambers (2017) considers a planet forming at 3 AU, accreting pebbles composed of rock and ice. The rock falls to the core, while the ice lodges in the envelope, subject to the constraint that at each depth, the partial pressure of water ice does not exceed the saturation vapor pressure. The goal is to determine the critical core mass of the planet (essentially the mass at which substantial gas accretion starts to occur) for an envelope enriched in heavy elements. The results show that this critical core mass falls in the range 2–5 M$_\oplus$, lower than the values obtained for envelopes of pure H/He, because of the higher mean molecular weight in the envelope. This effect was previously predicted by Stevenson (1984).

In the present paper, two formation scenarios are considered for Kepler-36 c, one in which the planet forms in situ at 0.128 AU, and the other in which it starts to form at an orbital distance of 1 AU, then migrates, during the later stages of formation, to its present orbit. The arguments for and against in situ models, as opposed to migration models, are summarized, along with relevant references, by Bodenheimer & Lissauer (2014) and D'Angelo & Bodenheimer (2016). The latter pa-

per shows that the masses and radii of all the planets in the Kepler-11 system, except Kepler-11 b, can be matched (with standard core accretion) either by an in situ model or by a migration model. After formation, our model planets are evolved, at constant heavy element mass, including mass loss from the H/He region of the envelope by XUV irradiation, up to the stellar age. We then compare models according to the standard core accretion theory with those calculated with the updated version, both for the in situ scenario and the migration scenario. With suitable choices for the initial surface density of solids in the disk and for the efficiency of mass loss, reasonable agreement with Kepler-36 c's observed mass and radius is found in all cases. For the case of Kepler-36 b, an updated formation calculation is performed in situ, leading eventually to complete loss of the hydrogen-helium part of the envelope, in agreement with the works quoted above.

2. COMPUTATIONAL METHOD

The calculations reported here use the following prescription for the deposition of heavy elements in the envelope. In all cases the planet forms inside the ice line, so that the planetesimals are composed of rock. As in Pollack et al. (1996), ablation and breakup are included during a planetesimal's passage through the envelope, and the amount of heavy elements deposited in each mass layer at each time step is calculated. Breakup turns out to be the main mechanism for mass deposition by accreting planetesimals. The criterion for breakup requires that the hydrodynamic (ram) pressure on the incoming planetesimal must exceed its compressive strength, which is provided by self-gravity as long as the radius of the object exceeds a few tens of km (e.g., D'Angelo & Podolak 2015)]. In practice, this criterion is met well above the surface of the solid/liquid core once the mass exceeds a few $M_\oplus$. For reasons discussed below, the heavy elements, now assumed to be vaporized, do not mix to uniform composition, but remain in the mass layer where they have been deposited. Then, starting at the surface and working inwards, a calculation determines, at a given layer, whether the partial pressure of the rock vapor ($P_{\rm part}$) exceeds the vapor pressure of rock at the surface temperature of a planetesimal in the layer. The vapor pressure (in dyne cm^{-2}) is given by

$$P_{\rm vap} = 3.92 \times 10^{13} \exp(-54700/T_s) \ , \qquad (1)$$

where T_s is the temperature of the surface layers of a planetesimal (D'Angelo & Podolak 2015). This expression is derived from data given in Melosh (2007). It is approximate for SiO_2 and does not distinguish among the different phases of what is actually a polymineralic assemblage, plausibly dominated by olivine or pyroxene. We ignore the likely presence of iron metal. Equation (1) does not distinguish whether the material is solid or liquid, but in practice the temperatures are such that liquid (or supercritical fluid) dominates the SiO_2 accreted after the envelope becomes sufficiently massive (even though the material arrives in the atmosphere as solid). The key features of our revised model are not sensitive to this choice of the vapor pressure curve, which could be wrong by an order of magnitude at some temperatures.

There is a wide range of estimates for the critical temperature ($T_{\rm crit}$) for rock vapor; for a summary see Melosh (2007). In our case it is set to 5000 K; if $T > T_{\rm crit}$, $P_{\rm vap}$ is essentially infinite. This means that "rock" and gas can mix in all proportions above the critical temperature. If $P_{\rm part} > P_{\rm vap}$, the excess heavy element material sinks to the mass zone below, leaving the considered layer saturated with rock vapor. The calculation continues all the way to the solid/liquid core, which can gain mass if the innermost zone satisfies $P_{\rm part} > P_{\rm vap}$. The result, during the main solid accretion phase, can be the structure of a "wet adiabat", on which the partial pressure of the heavy material is equal to the vapor pressure. Since, during this phase, the gas accretion rate is much less than the solid accretion rate (unlike the late-stage formation of giant planets), this prescription necessarily means that once the temperature reaches values for which the vapor pressure substantially exceeds the hydrogen pressure, the heavy element material that rains out differs little from the dense vapor immediately above – they are both essentially "rock". For example, a gas parcel that has a hydrogen/helium partial pressure of 1 bar (10^6 dyne cm^{-2}) at 5000 K will contain a rock partial pressure of 1.8×10^8 dyne cm^{-2} according to Equation (1), meaning the parcel is over 99% rock by mole fraction (and over 99.9% rock by mass). In reality, the thermodynamic behavior near criticality must be two coexisting phases, one of which is droplets of molten rock containing dissolved gas, and the other of which is a fluid hydrogen phase containing large amounts of evaporated (fluid) rock. In practice, the amount of hydrogen that dissolves into the rock rain-out is small. Thus, this model is largely indistinguishable from standard models with respect to the way the elements are distributed. The key differences are: (1) the accreted rock is much hotter (eventually supercritical), and (2) heat may not readily escape. For clarity of presentation, we refer to the *inner core* as the region that forms, during the earliest accretion stages, from silicate that arrives directly as solid or liquid, and the *outer core* as the almost pure silicate "vapor" (actually supercritical fluid upon compression), formed by breakup of planetesimals, that overlays it. In the following, we use $M_{\rm icore}$ and $R_{\rm icore}$ to refer to the mass and radius, respectively, of the *inner* core. Just outside the outer core, there is a layer, usually relatively thin, where the rock mass fraction strongly decreases with increasing radius. Above this region of non-uniform composition, the outer part of the planetary envelope consists essentially of H/He, with uniform solar composition.

The accretion rate of heavy elements (where M_Z is the total mass in heavy elements) is given by the standard equation (Safronov 1969)

$$\frac{dM_Z}{dt} = \dot{M}_Z = \pi R_{\rm capt}^2 \sigma \Omega F_g \ , \qquad (2)$$

where $R_{\rm capt}$ is the effective geometrical capture radius for planetesimals, σ is the mass per unit area of solid material (planetesimals) in the disk, Ω is the planet's orbital frequency, and F_g is the gravitational enhancement factor to the geometrical capture cross section. The planetesimal radius is taken to be 100 km, and F_g is taken from Greenzweig & Lissauer (1992). The planetesimal accretion rate is very high in the inner region of a protoplanetary disk, and the precise value of the planetesimal size or the uncertainty in the value of F_g have little effect on the outcome. In practice $R_{\rm capt} > R_{\rm icore}$, unless the envelope mass is negligible. The presence of the gaseous envelope enhances the capture radius, as determined by the procedures outlined in Podolak et al. (1988) and Pollack et al. (1996). The value of σ changes with time, taking into account the starting value for $M_{\rm core}$ as well as the heavy-element mass subsequently deposited onto the planet, and assuming that the feeding zone for solids includes the region within 4 Hill radii (R_H) inside and outside the planet's orbital semimajor axis (Kary & Lissauer 1994).

By the end of accretion, the inner (solid/liquid) core contains a relatively small fraction of the total mass; most of the accreted heavy elements remain in the outer core, as vapor or supercritical fluid with very small amounts of H/He. The inner core radius provides the inner boundary condition for the calculation of the structure of the envelope (which includes the outer core). Structure models for the inner core are calculated according to the procedure described in D'Angelo & Bodenheimer (2016). The cores are in hydrostatic equilibrium, assuming an adiabatic interior [see Equations (30) and (31) in that paper], and are composed of pure silicates. Given the inner core mass, and the temperature and pressure at the base of the envelope, the inner core radius $R_{\rm icore}$ is provided in a lookup table, based on those models. The temperature and pressure at the outer edge of the inner-core model match those at the base of the envelope.

The structure of the envelope is calculated under the assumption of hydrostatic equilibrium, spherical symmetry, and mass conservation. The basic structure equations are given by Kippenhahn & Weigert (1990). Added mass of heavy elements is deposited locally, as described above, and accreted H/He is added at the surface. If the planetesimals hit the inner core, which occurs only for a short time at the beginning of the calculation, the inner boundary condition for the luminosity is given by

$$L_{\rm accretion} \approx \frac{G M_{\rm core} \dot{M}_Z}{R_{\rm core}} \ . \qquad (3)$$

Otherwise, the luminosity is zero at the inner boundary. In that case, the mass and energy released by the accreted planetesimal are deposited at the breakup point and smeared over two pressure scale heights. The deposited energy in a given zone is given by Equation (10) of Pollack et al. (1996) and includes the latent heat of vaporization. The energy equation includes this energy source term, heating, cooling, contraction, expansion, and radiation from the surface.

In regions where the composition is uniform, the Schwarzschild criterion for convection is applied, and the adiabatic temperature gradient $\nabla_{\rm ad}$ is used. In the zones of the envelope where the composition is non-uniform, the Ledoux condition for convection is considered:

$$\frac{d\ln T}{d\ln P} > \left(\frac{d\ln T}{d\ln P}\right)_{\rm ad} - \frac{\chi_\mu \ d\ln \mu}{\chi_T \ d\ln P} \ , \qquad (4)$$

where μ is the mean molecular weight and

$$\chi_\mu \equiv \left(\frac{\partial \ln P}{\partial \ln \mu}\right)_{\rho,T} \qquad \text{and} \qquad \chi_T \equiv \left(\frac{\partial \ln P}{\partial \ln T}\right)_{\rho,\mu} \ . \qquad (5)$$

The structure of the layers of non-uniform composition is found to be stable against (ordinary) convection. In equilibrium models, the specific entropy increases significantly outwards in such zones, as a result, in part, of the steep outward decrease in the mean molecular weight (note that the "wet adiabat" does not have constant specific entropy). A further test was considered: take a point in a model where the ratio of mass fractions of H/He and rock vapor is, say, 1:1. Given the density ρ_1 and pressure P_1 at that point, adiabatically decompress that layer to the pressure (P_2) of a higher layer where the composition is all H/He (a finite displacement). The density $\rho_{\rm ad}$ after decompression is then compared with ρ_2, the model density at P_2. If $\rho_{\rm ad} > \rho_2$, then the region is stable against convection. All points that were tested in this manner, in the non-uniform region, turned out to be stable. The actual temperature gradient then must be less steep than that given by the left-hand side of Equation (4) but steeper than the adiabatic gradient, because the layers are unstable according to the Schwarzschild criterion. The actual value in such regions is uncertain; in most of our calculations it is taken to be 90% of the Ledoux condition. This condition is commonly met, except in layers where the composition gradient is very steep and nearly discontinuous, in which case the temperature gradient is set to less than the 90% value to allow numerical convergence. Temperature gradients in the non-uniform region can thus be much steeper than the adiabatic. Further, the energy transport in those layers is taken to be radiative, and no mixing of chemical composition through those layers is considered.

According to the evolutionary calculations of Leconte & Chabrier (2012), during the formation phase, slow mixing processes, such as double diffusive convection,

are likely to involve long time scales compared with the formation time and are therefore neglected. We also neglect these slow mixing processes during the cooling phase, although the much longer time scales during that phase suggest that at least some compositional mixing may well occur, depending on the parameters in the theory. The effect of these parameters on the degree of mixing should be examined in future work. It is common practice (e.g., in modeling the atmospheres of giant planets) to think of the "wet adiabat" as a convective state despite the compositional gradient. This state has a lower (i.e., less negative) temperature gradient than the dry adiabat because of the latent heat release that results in the upward adiabatic displacement of a saturated fluid element. In practice, this assumption of a convective state only makes sense if one thinks that there is perfect rain-out of condensate when a saturated parcel is lifted adiabatically. The conditions we encounter are enormously different from any of those considered in atmospheric dynamics because the compositional gradients are so large. It must be conceded that our understanding of these conditions is imperfect. There can be no doubt, however, that a supercritical mixture containing a compositional gradient cannot benefit from the latent heat release and rain-out, and its convective propensity is thus best assessed by the Ledoux criterion. Convective inhibition is further enhanced once the material is no longer an ideal gas, because the thermal effects on density are diminished then (i.e., $\alpha T < 1$, where α is the coefficient of thermal expansion).

The equation of state (EOS) in the envelope is taken from tables of the equation of state of SiO_2, mixed with various mass fractions of H/He, ranging from 0 to 1. In the case of pure H/He, the tables reduce to the equation of state of Saumon et al. (1995); the solar ratio of H to He is assumed. If there is a heavy element component, the tables are based on the quotidian EOS of More et al. (1988), as extended by Vazan et al. (2013). The tables have been compared with the results from the SESAME EOS (Lyon & Johnson 1992) and the ANEOS (Thompson & Lauson 1972), with good agreement.

The Rosseland mean opacity during the formation phase includes the effects of dust grains, as calculated by D'Angelo & Bodenheimer (2013) for the case of solar composition in the envelope. Tables are provided as a function of temperature and density, taking into account a number of grain species and a size distribution starting at 0.005 μm and ending at 1 mm. The number density N_g for grains goes as $N_g \propto r_g^{-3}$, where r_g is the grain radius. The grains are assumed to be carried in to the envelope by the accreted nebular gas. Once the grains evaporate, the gas opacities are taken from Ferguson et al. (2005) and Iglesias & Rogers (1996). A diagram of the opacities, when grains are present, is shown in D'Angelo & Bodenheimer (2016). At temperatures below 2000 K the molecular opacities (with no grains) of Freedman et al. (2008) are added to the grain opacity. They become significant only in the final isolated phase, after accretion stops, when the grains are assumed to settle into the interior and to evaporate. In the inner region of the envelope, where the composition is 100% rock vapor, a table is used with 100% heavy elements, taken from data in the Opacity Project archives (Seaton et al. 1994). The temperatures in the region where there is significant rock vapor are above 2000 K, and grains are not considered. Below 3600 K, the molecular opacities of Freedman et al. (2014) are used with a ratio of metals to hydrogen of 100 [their Equations (3), (4), and (5)]. Between 3600 K and 3900 K, opacities are interpolated between the values of Freedman et al. (2014) and those from the Opacity Project table. The high-metal opacities are high enough so that the regions of the models with 100% heavy elements are fully convective; therefore the structure is insensitive to the opacity values. In the transition region between 100% heavy elements and solar composition, which encompasses a small fraction of the mass, opacities are interpolated between the solar table and the high-Z table. The mass fraction of heavy elements is determined for a given zone, and logarithms of the opacities from these two tables are interpolated linearly in the mass fraction. A reduction in the assumed opacities, particularly at low temperature, would increase the rate at which the envelope could cool and therefore increase the gas accretion rate. Tests of the sensitivity of the results to the assumed opacities will be considered in future work.

The outer boundary conditions depend upon the phase of evolution. During the formation phase, nebular gas with solar composition is added to maintain the condition that the planet outer radius $R_p \approx R_{\rm eff}$, where $R_{\rm eff} = \min(R_B, 0.3R_H)$ and R_B and R_H are the Bondi radius and the Hill radius, respectively. The constant 0.3 is consistent with three-dimensional numerical simulations of disk flow and accretion near an embedded planet (Lissauer et al. 2009; D'Angelo & Bodenheimer 2013). During the formation phase, the temperature at R_p, $T_{\rm surf}$, is set to a constant value of 1000 K in the in situ scenario. In the migration scenario, during the solid accretion phase at 1 AU, $T_{\rm surf} = 500$ K. The density at R_p, $\rho_{\rm neb}$, is determined from the assumed disk surface density: $\rho_{\rm neb} = \sigma_g/(2H)$, where σ_g is the gas surface density in the disk, the scale height $H = 0.03\ a_p$ and, initially, $\sigma_g/\sigma_{\rm init} = 200$ (a_p is the distance of the planet from the star). The density σ_g, in the cases of fixed a_p, is assumed to decline linearly with time up to 3.3 Myr, when disk accretion cuts off. In all of these simulations, the envelope masses, which by our definition include the outer fluid core, become significantly larger than the inner core mass; nevertheless the phase of rapid gas accretion associated with the growth of Jupiter-mass planets never occurs. The important factor is the ratio of H/He mass to total heavy-element mass, which always remains small. During the isolation phase, photospheric boundary conditions are applied, including the

effects of irradiation from the central star; details are given in D'Angelo & Bodenheimer (2016), Equations (2) through (5). The equilibrium temperature $T_{\rm eq}$ at the orbit of Kepler-36 c is taken to be 928 K (with an assumed albedo of 0.3).

A detailed calculation of migration of the planet, coupled with the evolution of the protoplanetary disk, is beyond the scope of this paper but should be considered in future work. Thus, a very simple model is employed. Migration from 1 AU to 0.128 AU is assumed to take place on a characteristic time scale of 1.5×10^6 yr. This assumption is based on detailed calculations of migration of models of the Kepler-11 system in D'Angelo & Bodenheimer (2016). During the solid accretion phase (Phase 1), the formation time is very short compared with the migration time. Numerical experiments on the initial assembly of the core, based on a standard core accretion model (D'Angelo & Bodenheimer 2016) at 1 AU, taking into account the structure and evolution of the disk, show that by the time the core has accreted to 7 $M_\oplus$, its semimajor axis has decreased by about 10%. Thus, migration starts after the completion of this phase, shortly after the onset of Phase 2 (during which slow accretion of both gas and solids takes place), with $M_p \approx 7$ $M_\oplus$ and an elapsed time of $\approx 10^5$ yr. During migration, the surface temperature varies smoothly between 500 K and the ultimate $T_{\rm eq}$. The outer density $\rho_{\rm neb} \approx 4 \times 10^{-8}$ g cm^{-3} at 1 AU, then increases smoothly to 1×10^{-6} g cm^{-3} at 0.128 AU. During migration, gas accretion continues to occur according to the usual condition $R_{\rm p} = R_{\rm eff}$. The quantity $R_{\rm eff}$ decreases as the planet moves inward because of the decrease in R_H, which determines the outer boundary condition during this phase. The heavy element accretion rate is limited to a factor 2–3 less than the gas accretion rate, based on the results from Pollack et al. (1996) during Phase 2. The decrease in $R_{\rm p}$ can lead to mass loss from the H/He envelope under certain circumstances during this phase.

The isolation mass for the heavy-element component of a non-migrating planet is given by

$$M_{\rm iso} = \frac{8}{\sqrt{3}} (\pi C)^{3/2} M_\star^{-1/2} \sigma_{\rm init}^{3/2} a_p^3 \ , \qquad (6)$$

where $M_\star$ is the mass of the central star, and $C \approx 4$, the number of Hill-sphere radii defining the region, interior and exterior to the planetary orbit, from which the object is able to capture planetesimals (Lissauer 1987). Once $M_{\rm Z} \approx M_{\rm iso}$, the $dM_{\rm Z}/dt$ slows down drastically, but gas accretion continues. Thus, $\sigma_{\rm init}$ is chosen so that $M_{\rm iso} \approx M_p$, the present mass of the planet, but note that after $M_{\rm iso}$ is reached (which occurs before migration starts), the planet's mass will increase with addition of gas and solids during Phase 2, and will decrease with gas mass loss, possibly during migration and certainly during the isolation phase. The calculations thus assume that the accreted solids are present near the initial location of the growing planet; migration of solids from the outer disk in to the formation location is not considered, nor are possible changes in the accretion rate of solids caused by the planet's own migration (Alibert et al. 2005; D'Angelo & Bodenheimer 2016).

The rate of mass loss during the isolation phase, by irradiation of the planet by stellar X-ray and EUV photons, assumes energy-limited escape (Watson et al. 1981; Erkaev et al. 2007; Murray-Clay et al. 2009; Lopez et al. 2012) and is given by

$$\dot{M}_{\rm XUV} \approx -\frac{\epsilon \pi R_{\rm XUV}^3 F_{\rm XUV}}{K(\xi) G M_p} \ , \qquad (7)$$

where $R_{\rm XUV} \approx 1.1 R_p$ is the radius at which most of the stellar XUV flux is absorbed. The factor $K(\xi) = 1. - 3/(2\xi) + 1/(2\xi^3)$ corrects for the stellar tidal effect; $\xi = R_H/R_p$. The uncertain quantity $F_{\rm XUV}$ is taken from Ribas et al. (2005). This flux is most intense for time $t < 10^8$ yr and is given by $F_{\rm XUV} = 3 \times 10^{-4} L_\star/(4\pi a_p^2)$. After that time $F_{\rm XUV} = 3 \times 10^{-6} L_\star (5 \text{ Gyr}/t)^{1.23}/(4\pi a_p^2)$. Here, $L_\star$ is the stellar bolometric luminosity, which varies with time according to a theoretical stellar evolutionary track for $M_\star = 1.07$ $M_\odot$. The track is calculated with the program STELLAR (Bodenheimer et al. 2007); it starts in the pre-main-sequence phase at $t = 10^6$ yr and ends in the main-sequence phase at $t = 7$ Gyr, where it matches, within observational uncertainty, the present luminosity of Kepler-36. The generally assumed value of the efficiency factor $\epsilon = 0.1$, but other values, within about a factor 2, are considered.

At the time of disk dispersal, at the onset of the isolated phase, other mass-loss mechanisms have been suggested (Owen & Wu 2016; Ginzburg et al. 2016), driven basically by the loss of surface pressure from the disk. The outer radius of the planet in those studies is taken to be the Bondi radius; in our calculations for Kepler-36 c at disk dispersal, the actual radius, at 0.3 R_H, is a factor 10 smaller than R_B. The "Parker wind" mechanism (Owen & Wu 2016) is not effective at such a radius; however this possibility needs to be considered in detailed numerical simulations. For further discussion, see D'Angelo & Bodenheimer (2016), Section 2.3.

In summary, during the formation phase the following steps are taken during a time interval Δt: (1) calculation of mass and energy deposition by planetesimals, (2) calculation of rain-out and readjustment of mass and composition distributions, (3) solution of the full structure equations, given the updated composition distribution, (4) in migration calculations, adjustment of the planet's semimajor axis, and (5) addition (or possible subtraction) of H/He at the surface. During the isolation phase, at $a_p = 0.128$ AU, steps (2) and (3) are taken, and, in addition, XUV-induced mass loss from the outer H/He layers is computed. A full evolutionary sequence involves several thousand time steps Δt, of varying length.

3. CALCULATIONS AND RESULTS

The calculations start with an inner core mass of $M_{\rm icore} \approx 0.5$ M$_\oplus$ and negligible envelope mass. The negligible envelope mass at the outset is consistent with this core having formed quickly, since the associated accretion luminosity necessarily leads to a high basal temperature for this envelope (thousands of degrees). The ratio of the planets's outer radius (0.3 R_H for an in situ calculation) to core radius is accordingly only about eight, implying only about 3 orders of magnitude enhancement of the gas pressure at the (inner) core surface relative to the nebular pressure, insufficient to make an envelope mass that is a significant fraction of an Earth mass. Therefore, $M_{\rm env} \approx 3 \times 10^{-3}$ M$_\oplus$. The remainder of the formation phase is calculated, with accretion of gas and solids (planetesimals), up through the lifetime of the protoplanetary disk. Disk lifetimes are estimated to be a few Myr, with a range from roughly 1 to 10 Myr (Alexander et al. 2014). We arbitrarily take a value of 3.3 Myr. The transition is then made to an isolated (non-accreting) planet that evolves to the present state (7 Gyr) with evaporative mass loss of the H/He envelope as a consequence of XUV irradiation (e.g., Murray-Clay et al. 2009; Lopez et al. 2012).

The principal parameters are the surface density of solid material in the disk ($\sigma_{\rm init}$) at the time when the planet started to accrete, and the efficiency factor (ϵ) in the formula for the XUV mass loss. There are numerous other parameters involved in such simulations, including the equation of state, the radiative opacity, the form of the surface boundary condition, the treatment of zones with gradients in chemical composition, the details of the calculation of migration, and others. Here we do not do a systematic study of the effects of these parameters, but use values consistent with previous work, except for the consequences of the new physics (the possible dissolution of incoming planetesimals). We seek to establish the feasibility of explaining the properties of the planets with model fits using the new physics. The surface density is adjusted to obtain an approximate fit to the mass of the planet at 7 Gyr, and then the efficiency factor is fine-tuned to fit the radius, which also involves a small adjustment in the mass.

For the case of Kepler-36 c, four model sequences are considered: 0.128(Rev), 0.128(Old), 1.00(Rev) and 1.00(Old). The runs labelled (Rev) are calculated with mass deposition in the envelope as described in the previous section. The runs labelled (Old) assume, as in past calculations, e.g., D'Angelo & Bodenheimer (2016), that planetesimal material added to the envelope eventually sinks to the core, depositing mass and energy at the core surface. Otherwise, as far as possible, all other physical assumptions and parameters are the same in both types of runs. The runs labelled (0.128) assume that the planet forms in situ at 0.128 AU from the star, while the runs labelled (1.00) start the planet at 1 AU and migrate it to 0.128 AU while the protoplanetary disk is still present. The starting time ($t_{\rm start}$) for all runs depends on the time $t_{0.5}$ to build a core of 0.5 M$_\oplus$, as well as the time $t_{\rm pl}$ to form planetesimals of size 100 km. From Equation (2) we estimate $t_{0.5} \approx 10^3$ yr at 1 AU, and it is even shorter at 0.128 AU. The time $t_{\rm pl}$ is unknown, but could well be longer than 10^3 yr; it depends on the detailed evolution of dust and gas in the disk. We arbitrarily set $t_{\rm start} = 2 \times 10^3$ yr (for all runs); its precise value has practically no effect on the results and conclusions of this paper. The cutoff time for accretion from the disk is about 3.3 Myr in all cases, and migration in the (1.00) runs starts shortly after the isolation mass has been reached, at $t \approx 10^5$ yr.

The parameters and basic results for the runs are given in Table 1. The column headings in the table give the run identifiers. The first two rows below the run identifiers give the initial assumed surface density of solid material ($\sigma_{\rm init}$) in the disk, and the value of ϵ in Equation (7). The initial gas surface density σ_g in all cases is 200 times $\sigma_{\rm init}$. Note the very high values of $\sigma_{\rm init}$ that are required to fit the mass of the present planet in the case of the in situ runs. The values are about 9 times higher than the corresponding surface density (Chiang & Laughlin 2013) in the typical minimum-mass extrasolar nebula (MMEN; their Equation 4). Note, however, that such a disk would still be gravitationally stable (see Figure 14 of D'Angelo & Bodenheimer 2016). In the case of the migration models, the assumed values of $\sigma_{\rm init}$ are about 4 times higher than the corresponding ones in the MMEN.

The bottom 12 rows give results: the final values of time ($\approx$ 7 Gyr), final planet total mass M_p, the mass in the inner core of heavy elements $M_{\rm icore}$, for (Rev) models, along with the entire core mass $M_{\rm core}$, for (Old) models, the final mass of heavy elements $M_{\rm Z}$ in the envelope, the total mass in H/He at the time of disk cutoff (3.3 Myr), the final total mass ($M_{\rm XY}$) in H/He, the final total mass in the envelope $M_{\rm env}$, including both heavy elements and H/He, the final temperature $T_{\rm icb}$, for (Rev) models, at the inner core boundary, along with the corresponding temperature $T_{\rm cb}$, for (Old) models, at the outer edge of the entire core, the final density $\rho_{\rm icb}$, for (Rev) models, at the inner core boundary, along with the corresponding density $\rho_{\rm cb}$, for (Old) models, at the outer edge of the entire core, the final mean density of the inner core ($\bar{\rho}_{\rm icore}$), for (Rev) models, along with the final mean density of the entire core ($\bar{\rho}_{\rm core}$), for (Old) models, the final outer radius, and the final value of the intrinsic luminosity ($L_{\rm int}$).

3.1. *In situ model: Run 0.128(Rev)*

Masses and radius as a function of time for Run 0.128(Rev) are shown in Figure 2. The calculation starts with $M_{\rm icore} = 0.40$ M$_\oplus$, $M_{\rm env} = 2.2 \times 10^{-4}$ M$_\oplus$, with the envelope composed entirely of H/He. In the preliminary phase of formation, the core accretes to 1.3 M$_\oplus$

Table 1. Input Parameters and Results

Run →	0.128(Rev)	0.128(Old)	1.00(Rev)	1.00(Old)
Disk solid $\sigma_{\rm init}$ (g cm^{-2})	1.18×10^4	1.085×10^4	196	190
ϵ for $\dot{M}_{\rm XUV}$	0.08	0.22	0.04	0.18
Final time (Gyr)	7.01	7.05	7.03	7.02
Final M_p (M$_\oplus$)	7.80	7.68	7.81	8.01
Final $M_{\rm icore}$ or $M_{\rm core}$ (M$_\oplus$)	1.30	7.00	1.87	7.32
Final env. $M_{\rm Z}$ (M$_\oplus$)	6.13	–	5.65	–
Disk cutoff $M_{\rm XY}$ (M$_\oplus$)	1.13	2.21	0.67	1.40
Final $M_{\rm XY}$ (M$_\oplus$)	0.37	0.68	0.29	0.69
Final total $M_{\rm env}$ (M$_\oplus$)	6.50	0.68	5.94	0.69
Final $T_{\rm icb}$ or $T_{\rm cb}$ (K)	1.75×10^4	2.20×10^3	1.54×10^4	2.22×10^3
Final $\rho_{\rm icb}$ or $\rho_{\rm cb}$ (g cm^{-3})	8.00	0.46	7.59	0.46
Final $\bar{\rho}_{\rm icore}$ or $\bar{\rho}_{\rm core}$ (g cm^{-3})	8.55	6.59	8.35	6.38
Final radius (R$_\oplus$)	3.66	3.74	3.72	3.72
Final log ($L_{\rm int}$/L$_\odot$)	-10.85	-12.51	-10.78	-12.56

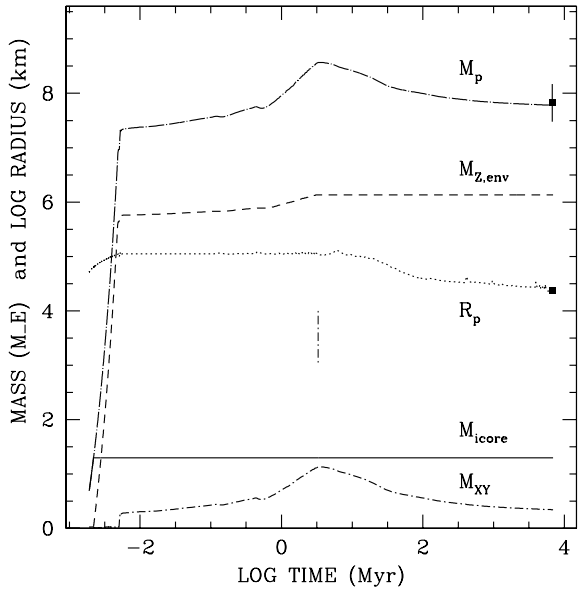

Figure 2. Evolution of Run 0.128(Rev). Upper (long dash-dot) curve: total mass M_p (in M$_\oplus$); dashed curve: total heavy-element mass in the envelope $M_{\rm Z,env}$; dotted curve: outer log radius R_p (in km); solid curve: heavy-element inner core mass $M_{\rm icore}$; short dash-dot curve: hydrogen/helium mass in the envelope $M_{\rm XY}$; vertical dash-dot line: time of disk accretion cutoff. The observed mass of Kepler-36 c, with error bars at 84% confidence level, and the observed radius, are given as filled squares.

in a time of only a few hundred years at the rapid solid accretion rate in the inner disk. Up to that point, a small amount of heavy elements lands in the envelope through ablation, and some H/He is accreted, giving $M_{\rm Z,env} = 2.81 \times 10^{-2}$ M$_\oplus$ and $M_{\rm XY} = 9.85 \times 10^{-3}$ M$_\oplus$. Beyond that point, breakup of the planetesimals takes place in the envelope, no further accretion onto the inner core takes place, and all the accreted planetesimals remain in the envelope. The radiated luminosity during this phase is 10^{-6} to 10^{-5} L$_\odot$, generally only 5–10% of the rate of energy deposition by planetesimals. The planetesimals release their energy interior to the layer where the sharp molecular weight gradient occurs, and because of the limited energy transport across that layer, much of the deposited energy goes into heating and expansion of the inner (high-Z) regions. During this solid accretion phase, the structure is fully convective except in the layers with a composition gradient. The convective structure is associated with the high nebular density ($\approx 2\times10^{-5}$ g cm^{-3}) and high nebular temperature (1000 K) for the in situ case. An example of the structure during the solid accretion phase is shown in Figure 3. The partial pressure of the rock vapor, the mass fraction of the rock vapor, and the vapor pressure are plotted as a function of temperature. An example of total pressure as a function of temperature during this phase is shown in Figure 4, emphasizing very steep composition and temperature gradients in the layers where the mean molecular weight changes rapidly. In other regions, the gradient is adiabatic.

By the time of 5×10^3 yr, all of the solid material in the feeding zone has been accreted, and Phase 2 starts. At this time, the masses are: $M_{\rm icore} = 1.3$, $M_{\rm Z,env} = 5.64$, and $M_{\rm XY} = 0.027$, all in Earth masses. The growth rate drops drastically as the planet enters Phase 2. During this phase, the heavy-element mass increases at roughly half the rate of H/He mass. In this connection, Pollack et al. (1996) show that the accretion rate of solids ($\dot{M}_{\rm Z}$)

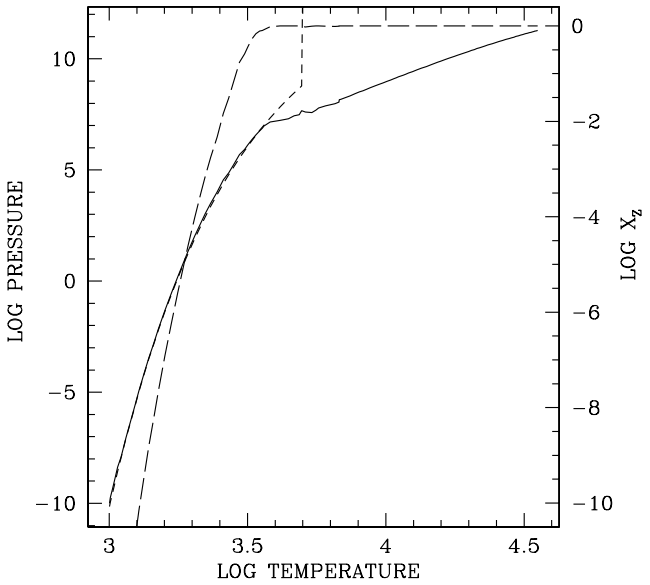

Figure 3. Structure of a model in Run 0.128(Rev) at a time (during the runaway solids accretion epoch in Phase 1) when $M_{\rm icore} = 1.3$ M$_\oplus$, heavy-element mass in the envelope $M_{\rm Z,env} = 1.15$ M$_\oplus$, and hydrogen/helium mass in the envelope $M_{\rm XY} = 1.4 \times 10^{-2}$ M$_\oplus$. Solid curve (left scale): partial pressure of the silicate vapor; short-dashed curve (left scale): vapor pressure for the silicates; long-dashed curve (right scale): mass fraction (X_Z) of silicate vapor. Pressures are given in dyne cm^{-2}, temperatures in K. Above the critical temperature (uncertain but assumed to be 5000 K) the vapor pressure is assumed to become very high.

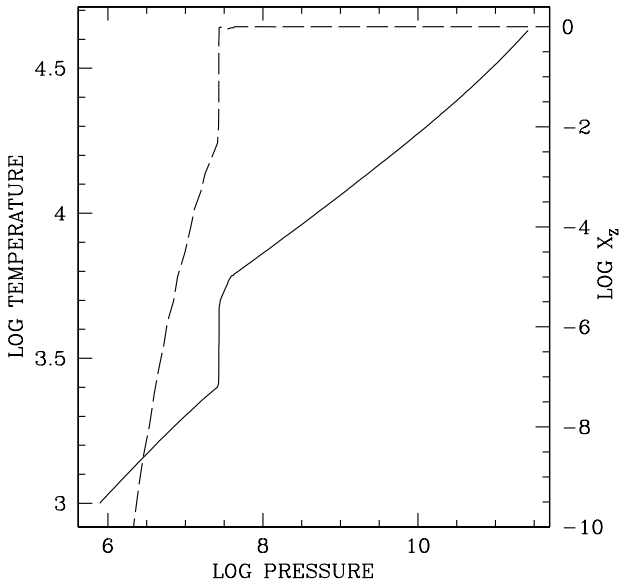

Figure 4. Structure of a model in Run 0.128(Rev) at a time when $M_{\rm icore} = 1.3$ M$_\oplus$, heavy-element mass in the envelope $M_{\rm Z,env} = 2.37$ M$_\oplus$, and hydrogen/helium mass in the envelope $M_{\rm XY} = 2.5 \times 10^{-2}$ M$_\oplus$. Solid curve (left scale): temperature (K) as a function of total pressure (dyne cm^{-2}); dashed curve (right scale): mass fraction (X_Z) of silicate vapor. Note the very steep temperature and composition gradients at log pressure = 7.5.

in this phase is related to the accretion rate of gas ($\dot{M}_{\rm XY}$) by (their Equation 17)

$$\dot{M}_{\rm Z} \approx \left(2 + 3\frac{M_{\rm XY}}{M_{\rm Z}}\right)^{-1} \dot{M}_{\rm XY} \ . \qquad (8)$$

At the beginning of the phase, this expression gives a H/He accretion rate twice as fast as the heavy-element accretion rate. At the end of the phase, when $M_{\rm XY}$ has increased to 1.13 M$_\oplus$, the ratio is closer to 2.5, in reasonable agreement with the numerical results.

At the beginning of Phase 2 there is a brief readjustment, as the central regions, no longer supported by energy deposition from planetesimals, and still radiating at a rate controlled by the properties of the region of non-uniform composition, contract significantly. The density $\rho_{\rm icb}$ (at the inner core boundary) increases from 0.6 to 3.6 g cm^{-3}, and there is a brief burst in luminosity (to $\approx 10^{-3}$ L$_\odot$) as the entire structure is forced to contract. Thereafter, the luminosity declines rapidly and remains at a typical value of $10^{-7.5}$ L$_\odot$ through Phase 2. As a result of the reduced luminosity, a radiative zone develops in the outer layers, reaching inward to a temperature of 2000 K and to a radius about half the outermost value, encompassing about 1% of the total envelope mass (7% of $M_{\rm XY}$). Disk cutoff occurs at 3.3×10^6 years with $M_{\rm Z,env} = 6.13$ and $M_{\rm XY} = 1.13$ M$_\oplus$, and with $R_p = 17.7$ R$_\oplus$ (1.12×10^{10} cm). The temperature $T_{\rm icb}$ (just outside the inner core boundary) is 6.3×10^4 K; the density (at the same point) is 2.7 g cm^{-3}. The composition is uniform with 100% Z out to a temperature $T = 2.08 \times 10^4$ K and radius 2.08×10^9 cm, decreasing to 95% at $T = 1.90 \times 10^4$ K at essentially the same radius, to 50% at $T = 1.00 \times 10^4$ K at radius 2.44×10^9 cm, and to 1% at $T = 3000$ K, radius 4.62×10^9 cm. The structure of the model shortly after the cutoff is shown in Figure 5. The outer radiative zone remains, extending inward to a temperature of 1500 K.

During the isolated phase, the parameter ϵ in Equation (7) is set to 0.08. Initially, the high internal energy and average intrinsic luminosity around 10^{-9} L$_\odot$ combine to give a cooling time of $\approx 10^8$ yr. During the first 10^8 yr, when the rate of mass loss is high, the radius decreases by a factor 2.6, and 0.56 M$_\oplus$ of H/He is lost by photoevaporation ($\dot{M}_{\rm XUV} \approx 10^{-9}$ M$_\oplus$ yr^{-1} at that time). Later, the intrinsic luminosity declines to $\approx 10^{-11}$ L$_\odot$, the internal temperature cools by a factor of ≈ 4, the cooling time increases by an order of magni-

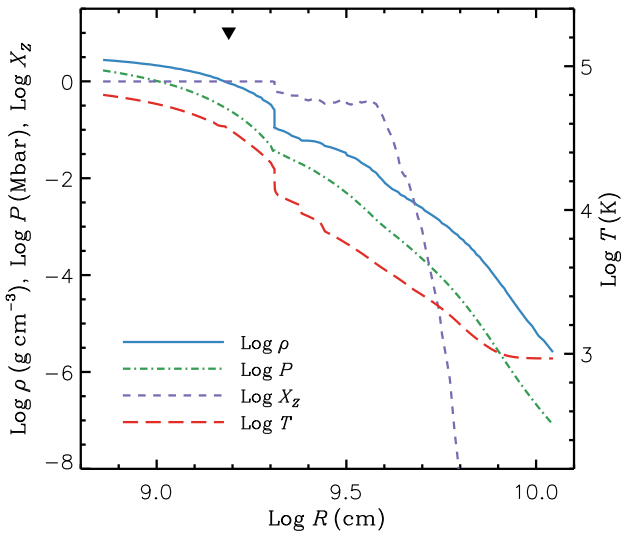

Figure 5. Structure of the model in Run 0.128(Rev) at time 4.7 Myr, soon after the beginning of the isolated phase of evolution. Solid curve (left scale): log density in g cm^{-3}; dash-dot curve (left scale): log pressure in Mbar; long-dashed curve (right scale): log temperature in K; short-dashed curve (left scale): log X_Z, the log of the mass fraction of heavy elements. Filled triangle: the half-mass point in the envelope. The mean density of the inner core is 5.62 g cm^{-3}. The energy transport is mainly by convection; the layers outside log r = 9.8 are radiative. The section of X_Z between log r = 9.3 and log r = 9.6 is a relic of Phase 2, during which the accretion rate of H/He is 2 to 2.5 times greater than the solid accretion rate.

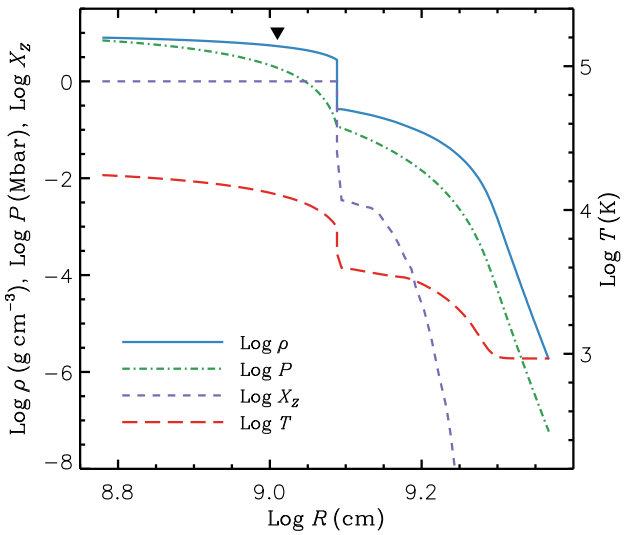

Figure 6. Structure of the model in Run 0.128(Rev) at time 7.01 × 10^9 yr. Symbols and curves as in Figure 5. The mean density of the inner core is 8.55 g cm^{-3}.

tude, and the rate of mass loss declines significantly, by 2.5 orders of magnitude to 3 × 10^{-12} M$_\oplus$ yr^{-1} by the final time.

Between $t = 10^8$ yr and $t = 7\times10^9$ yr an additional 0.2 M$_\oplus$ is lost. The final model planet, whose mass and radius agree quite well with that of the actual planet, has a total heavy element mass (including the inner core) of M_Z = 7.43 M$_\oplus$ and H/He mass M_{XY} = 0.37 M$_\oplus$. The structure is still largely convective, with an outer radiative zone including less than 1% of the mass. The actual luminosity of the planet is completely dominated by the re-radiation of stellar luminosity at the equilibrium temperature, which gives log (L/L$_\odot$) decreasing from −4.9 to −6.1 as the planet contracts during the isolation phase. This range holds for all cases discussed here. The structure of the final model is shown in Figure 6.

3.2. *In situ model: Run 0.128(Old)*

Run 0.128(Old) starts in situ at σ_{init} = 1.085 × 10^4 g cm^{-2}, slightly lower than that in Run 0.128(Rev). The masses and radius as a function of time are given in Figure 7.

At first, the total core mass (M_{core}) increases very rapidly until it reaches 6.27 M$_\oplus$, close to the isolation mass. At this point the M_{env} = 0.34 M$_\oplus$. The temperature T_{cb} (at the base of the envelope) is 1.03 × 10^4 K, much lower than the value of T_{icb} = 5.8 × 10^4 K reached at a comparable evolutionary phase in Run 0.128(Rev). The structure is fully convective at this point.

During the subsequent Phase 2, M_{core} increases by 0.73 and M_{env} by 1.87 M$_\oplus$. The typical luminosity is 10$^{-7.5}$ L$_\odot$, about the same as in Run 0.128(Rev) during the same phase. As in Run 0.128(Rev), a radiative zone develops in the outer region, extending inward to T = 2000 K. Disk cutoff occurs at time 3.3 Myr, with radius 17.5 R$_\oplus$, T_{cb} = 9430 K, pressure at the core boundary P_{cb} = 0.245 Mbar, and density ρ_{cb} = 0.271 g cm^{-3}. All of these values are factors of a few lower than those in Run 0.128(Rev) at the inner core boundary at disk cutoff. The core and envelope masses are, respectively, 7.0 and 2.21 M$_\oplus$. The structure is plotted in Figure 8.

By the time of disk cutoff, this run was able to accrete twice as much H/He as was possible for Run 0.128(Rev) at the same time. The mean density of the inner plus outer cores in Run 0.128(Rev), during the main phase of gas accretion, is a factor 20 to 30 lower (with a correspondingly larger radius) than the core density in Run 0.128(Old).

At the beginning of the isolated phase, the cooling time is ≈ 5 × 10^7 yr; the mass loss efficiency factor is set to 0.22. At an age of 10^8 yr, the temperature T_{cb} has decreased to 5.96 × 10^3 K and M_{env} to 1.28 M$_\oplus$, a loss

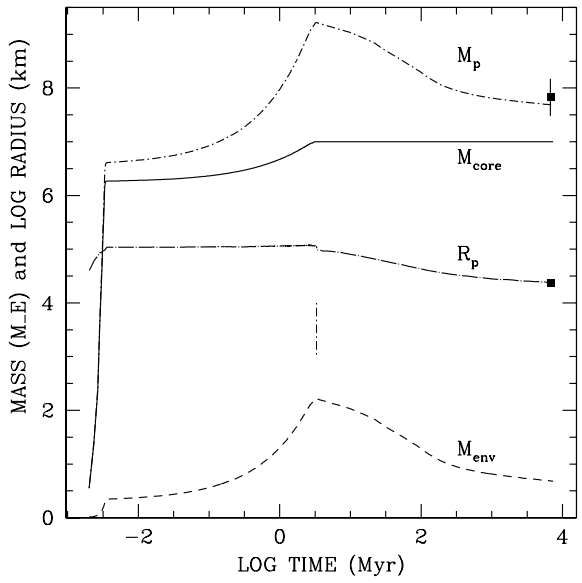

Figure 7. Evolution of Run 0.128(Old). Upper (short-dash dot) curve: total mass M_p (in $M_\oplus$); solid curve: core mass $M_{\rm core}$; long-dash dot curve: outer log radius R_p; dashed curve: hydrogen/helium mass in the envelope $M_{\rm env}$; vertical dash-dot line: time of disk accretion cutoff. The observed mass of Kepler-36 c, with error bars at 84% confidence level, and the observed radius, are given as filled squares.

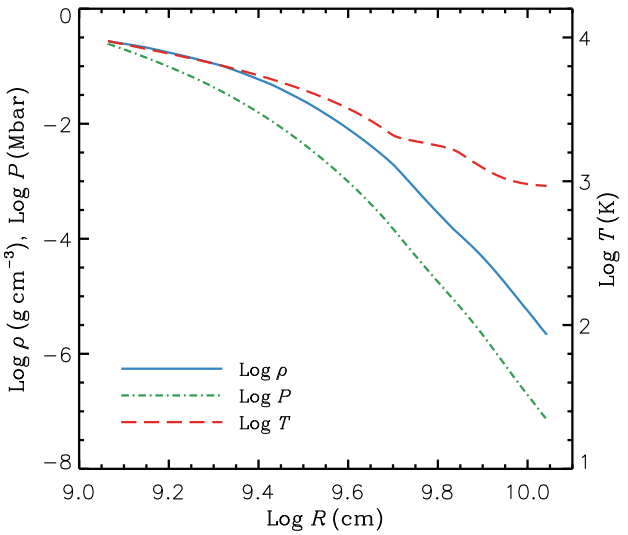

Figure 8. Structure of the H/He envelope in Run 0.128(Old) at time 3.3 Myr (disk cutoff). Solid curve (left scale): log density as a function of radius; dash-dot curve (left scale): log pressure as a function of radius; dashed curve (right scale): log temperature as a function of radius. The mean density of the core is 6.42 g cm^{-3}. The structure is radiative outside log $r = 9.7$; otherwise convective.

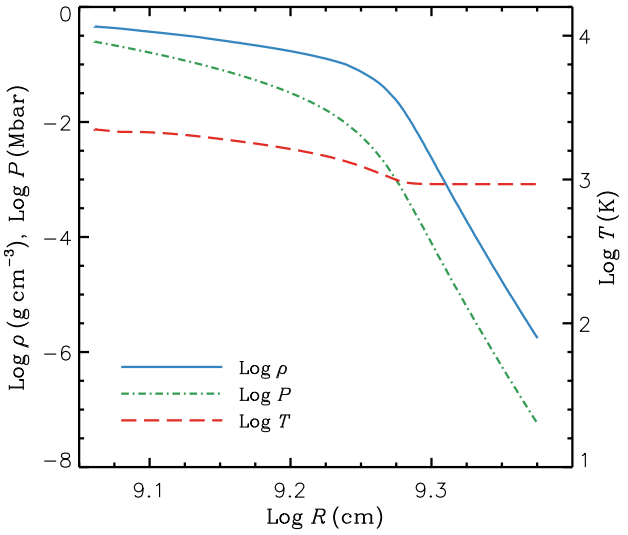

Figure 9. Structure of the H/He envelope in Run 0.128(Old) at time 7.05×10^9 yr (final model). Curves as in Figure 8. The mean density of the core is 6.59 g cm^{-3}.

of 0.93 $M_\oplus$. An additional 0.60 $M_\oplus$ is lost up to the end of evolution at 7.05×10^9 yr. Near the beginning of the isolated phase, the intrinsic luminosity, representing the cooling of the planet, is log $(L/L_\odot) = -8.5$, decreasing to log $(L/L_\odot) = -12.5$ at the final time.

The final model (Figure 9) has a radius of 3.74 $R_\oplus$, close to the upper limit of the error bar for the planet (Deck et al. 2012). The mass is 7.68 $M_\oplus$, in good agreement with that of the planet. The temperature $T_{\rm cb}$ has decreased to 2.23×10^3 K by this time, much cooler than the value of $T_{\rm icb} = 1.75 \times 10^4$ K at the end of Run 0.128(Rev). As a result of the very low luminosity, the structure is fully radiative by this point.

In Run 0.128(Old) much more H/He accretes into the envelope (2.21 $M_\oplus$) up to disk cutoff, as compared with Run 0.128(Rev) (1.13 $M_\oplus$). The reason is that the outer core region of the revised model is much hotter and less dense than are the corresponding mass elements in the old model. Thus, in order to reduce $M_{\rm XY}$ to the point where the radius agrees with that of the planet, a higher mass loss efficiency parameter, by over a factor of 2, is required. Alternatively, we could have reduced the assumed lifetime of the disk and slightly increased $\sigma_{\rm init}$. Also, the old model, as a consequence of its lower total thermal energy, contracts faster than the revised one, reducing $\dot{M}_{\rm XUV}$ in comparison with the revised model. To reduce the value of the required ϵ, one must change some other parameter, such as the ratio of the outer radius R_p to R_H (or the lifetime of the gas in the protoplanetary disk). A run was completed with $R_p/R_H = 0.25$ as compared with the normal value of 0.3. The main effect is reduction of the accreted $M_{\rm XY}$ into the envelope.

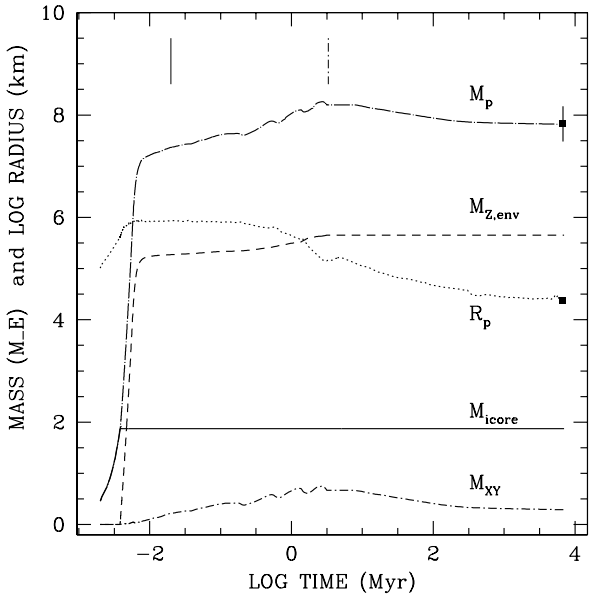

Figure 10. Evolution of Run 1.00(Rev). Upper (long dash-dot) curve: total mass M_p (in $M_\oplus$); dashed curve: total heavy-element mass in the envelope $M_{\rm Z,env}$; dotted curve: outer log radius R_p (in km); solid curve: heavy-element inner core mass $M_{\rm icore}$; short dash-dot curve: hydrogen/helium mass in the envelope $M_{\rm XY}$; thin vertical solid line: time of onset of migration; thin vertical dash-dot line: time of disk accretion cutoff. The observed mass of Kepler-36 c, with error bars at 84% confidence level, and the observed radius, are given as filled squares.

However, given the same solid surface density, the total mass is reduced and there is a compensating effect: the smaller radius results in slower mass loss during the isolation phase. The end result was a model whose radius ($R_p = 3.73$ R$_\oplus$) agrees well with that of the planet, and whose mass (7.49 M$_\oplus$) falls just within the error bar. However, the efficiency factor, adjusted to give the correct radius, has declined only slightly, from 0.22 to 0.18.

3.3. *Migration model: Run 1.00(Rev)*

Masses and radius as a function of time for Run 1.00(Rev) are shown in Figure 10. The calculation starts with $M_{\rm icore} = 0.46$ M$_\oplus$, $M_{\rm env} = 5.4\times10^{-4}$ M$_\oplus$, with the envelope composed almost entirely of H/He. At first, the core accretes to 1.81 M$_\oplus$ in a time of 1350 years, with a solid accretion rate $\approx 10^{-3}$ M$_\oplus$ yr^{-1}. At that point, $M_{\rm Z,env} = 1.5\times10^{-6}$ and $M_{\rm XY} = 3\times10^{-3}$ M$_\oplus$. Planetesimals continue to accrete onto the core until it reaches $M_{\rm icore} = 1.87$ M$_\oplus$. Beyond that point, breakup of the planetesimals takes place in the envelope, $M_{\rm icore}$ remains constant, and all the accreted heavy elements remain in the envelope, forming the outer core. During this phase, planetesimals are deposited in the inner regions at radius $R_{\rm dep}$, inside the layer where the steep composition gradient occurs, at $R_{\rm dcont}$. For example, when the total envelope mass $M_{\rm env} = 1.5$ M$_\oplus$, $R_{\rm dep} = 5.29$ R$_\oplus$, $R_{\rm dcont} = 6.2$ R$_\oplus$, while $R_{\rm icore} = 1.31$ R$_\oplus$. Also, when $M_{\rm env} = 2.67$ M$_\oplus$, $R_{\rm dep} = 7.13$ R$_\oplus$, $R_{\rm dcont} = 8.2$ R$_\oplus$, at the same $R_{\rm icore}$. Only a fraction of the energy liberated at $R_{\rm dep}$ can be radiated through $R_{\rm dcont}$, and much of the deposited energy goes into heating and expansion of the inner regions. For example, the luminosity radiated at the surface can be as low as 1% of the rate of energy deposition in the interior. This ratio varies with time. Interior and exterior to the layer with the gradient, however, the structure is convective.

At the time of 1×10^4 yr, practically all planetesimals available in the feeding zone have been accreted, and Phase 2 starts. At this time, the masses are: $M_{\rm icore} = 1.87$, $M_{\rm Z,env} = 5.26$, $M_{\rm XY} = 0.14$, and $M_p = 7.27$, all in Earth masses. The outer radius is $R_p = 133$ R$_\oplus$, as determined by 0.3 R_H. The structure at this time is shown in Figure 11. As in previous cases, an outer radiative zone develops.

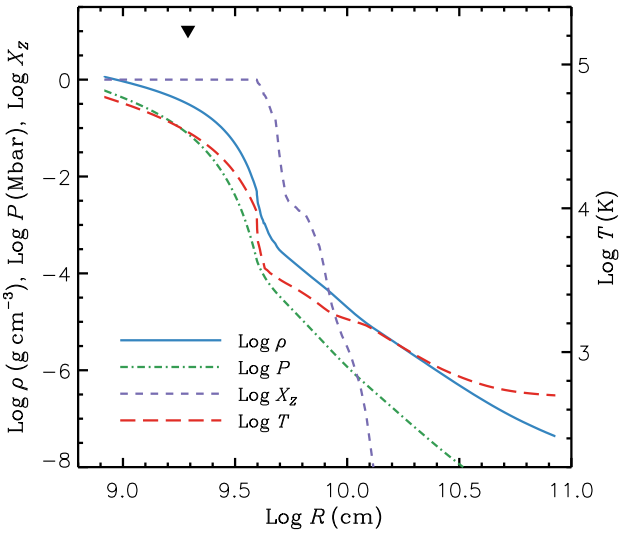

Figure 11. Structure of the model in Run 1.00(Rev) at time 1×10^4 yr, at 1 AU just before the onset of migration. Solid curve (left scale): log density in g cm^{-3}; dash-dot curve (left scale): log pressure in Mbar. The surface value (not plotted) is 7.56×10^{-4} bar. Long-dashed curve (right scale): log temperature in K; short-dashed curve (left scale): log $X_{\rm Z}$, the log of the mass fraction of heavy elements. Filled triangle: the half-mass point in the envelope. The mean density of the inner core is 4.63 g cm^{-3}. Note that the composition curve at log $r = 9.7$ is practically discontinuous; it is resolved by a few grid points. Interior to that point, the model is convective; outside log $r = 9.91$ it is radiative.

Shortly after this time, migration starts. The rate of accretion of solids plays a much smaller role in the overall energy budget during this phase, which is dominated by contraction and accretion of H/He. As discussed in Section 2, the simple migration model neglects the fact that the planet is migrating into a region that hasn't been mostly cleared of planetesimals by the planet's own accretion (although the prior formation and migration of Kepler-36 b should have done some clearing). The growth time scale increases drastically to O(10^6) yr, with heavy-element mass increasing at roughly half the rate of H/He mass. At $t = 0.8$ Myr, $a_p = 0.6$ AU, R_p has decreased to 78 $R_\oplus$, $M_{\rm Z,env} = 5.46$ $M_\oplus$, and $M_{\rm XY} = 0.57$ $M_\oplus$. The H/He content reaches a maximum at $t = 2.7 \times 10^6$ yr when $a_p = 0.17$ AU and $M_{\rm XY} = 0.75$ $M_\oplus$. Beyond that point, $M_{\rm XY}$ decreases as a result of Roche-lobe overflow because of the decreasing value of R_H. The luminosity during this phase declines gradually from $10^{-6.5}$ to $10^{-8.5}$ $L_\odot$ as a result of the decreasing accretion rate of gas and solids as the value of the Hill radius decreases. Disk cutoff occurs at 3.3×10^6 years with $M_{\rm Z,env} = 5.65$ and $M_{\rm XY} = 0.67$ $M_\oplus$, and with $R_p = 18$ $R_\oplus$ (1.18×10^{10} cm). The temperature $T_{\rm icb} = 6.36 \times 10^4$ K; the density $\rho_{\rm icb} = 1.47$ g cm^{-3}. The composition is uniform with 100% silicates out to a temperature $T = 2.1 \times 10^4$ K and radius 2.72×10^9 cm, decreasing to 50% at $T = 5.42 \times 10^3$ K and radius 3.39×10^9 cm, and to 1% at $T = 2960$ K and radius 4.84×10^9 cm.

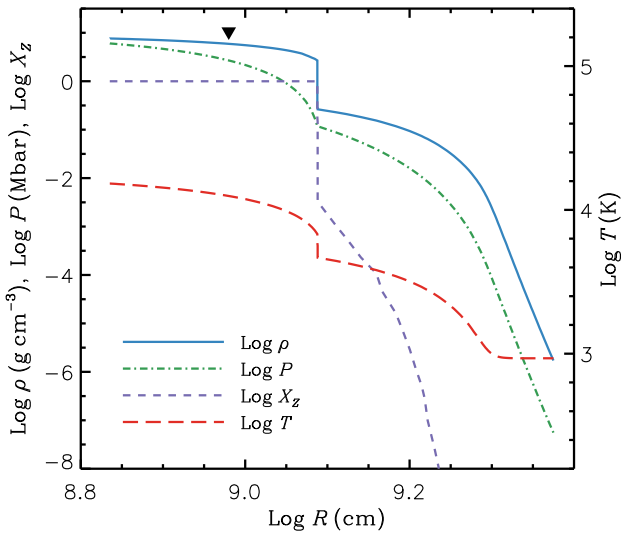

Figure 12. Structure of the model in Run 1.00(Rev) at time 7.03×10^9 yr. Symbols and curves: as in Figure 11. The mean density of the inner core is 8.35 g cm^{-3}.

During the isolated phase, the parameter ϵ in Equation (7) is set to 0.04. During the first 10^8 yr, an additional 0.25 $M_\oplus$ is lost, giving $M_{\rm XY} = 0.42$ $M_\oplus$, $R_p = 7.43$ $R_\oplus$, $L = 2.0 \times 10^{-10}$ $L_\odot$, and a cooling time of 8×10^8 yr. At this time, $\dot{M}_{\rm XUV} \approx 8.8 \times 10^{-10}$ $M_\oplus$ yr^{-1}. As in Run 0.128(Rev), a radiative zone extends inward to $T = 1500$ K. Later, the luminosity declines to $\approx 10^{-11}$ $L_\odot$, the cooling time increases by an order of magnitude, and the rate of mass loss declines significantly, by a factor 400, to 2×10^{-12} $M_\oplus$ yr^{-1}, by the final time. Between $t = 10^8$ yr and $t = 7 \times 10^9$ yr a further 0.13 $M_\oplus$ is lost from the H/He envelope. The radius of the final model planet agrees quite well with that of the actual planet, as does the total mass. The total heavy element mass (including the inner and outer cores) is $M_{\rm Z} = 7.52$ $M_\oplus$, and the H/He mass $M_{\rm XY} = 0.29$ $M_\oplus$. The inner core of 1.87 $M_\oplus$ has $R_{\rm icore} = 1.075$ $R_\oplus$ and mean density 8.35 g cm^{-3}. The region of almost 100% heavy elements has radius 1.84 $R_\oplus$, and the mean density of the inner plus outer cores is 5.86 g cm^{-3}.

The mass of this final model is very close to that of the in situ model 0.128(Rev). The temperature at the boundary between the inner and outer cores ($T_{\rm icb}$) is similar (1.54×10^4 K vs. 1.75×10^4 K), and the corresponding density is slightly lower (7.59 vs. 8.0 g cm^{-3}). These differences are presumably caused primarily by the different masses of the inner cores. Both final models have outer radiative zones, extending inward to $T = 1850$ K in the in situ case and to 1500 K in the present case; they include less than 1% of the envelope mass. The structure of the final model for Run 1.00(Rev) is plotted in Figure 12.

3.4. *Migration model: Run 1.00(Old)*

Run 1.00(Old) starts at 1 AU with $\sigma_{\rm init} = 190$ g cm^{-2}, slightly lower than that in Run 1.00(Rev). Outer densities and temperatures are the same in the two runs. The masses and radius as a function of time are given in Figure 13. At first, $M_{\rm core}$ increases very rapidly until, at $t \approx 7 \times 10^3$ yr, it reaches 6.78 $M_\oplus$, close to the isolation mass of 6.81 $M_\oplus$. At this point, $M_{\rm env} = 0.084$ $M_\oplus$. The temperature $T_{\rm cb}$ is 9.91×10^3 K, much lower than the value of $T_{\rm icb} = 6.1 \times 10^4$ K reached at a comparable evolutionary phase in Run 1.00(Rev). The lower mean molecular weight in the H/He envelope accounts for much of this difference. The luminosity during the solid accretion phase averages about 10^{-4} $L_\odot$, corresponding to a mass accretion rate onto the core of 1 to 1.5×10^{-3} $M_\oplus$ yr^{-1}. Essentially all the energy deposited by the planetesimals is radiated away. The structure is fully convective during this phase.

Migration starts slightly later, with $M_{\rm core} = 7.04$, $M_{\rm env} = 0.63$ $M_\oplus$, and $R_p = 137.6$ $R_\oplus$ (as determined by 0.3 R_H). The structure of the model at this point is shown in Figure 14; an outer radiative zone has developed. At $t = 0.8$ Myr, the planet has $a_p = 0.67$ AU with $M_{\rm core} = 7.17$ $M_\oplus$, $M_{\rm env} = 1.02$ $M_\oplus$, and $R_p = 92.2$ $R_\oplus$. The luminosity during this phase declines gradually from $10^{-6.5}$ to 10^{-8} $L_\odot$ as the accretion rate of gas

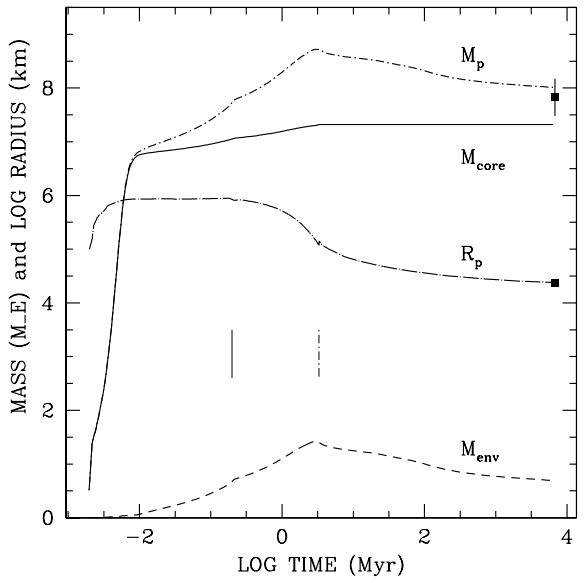

Figure 13. Evolution of Run 1.00(Old). Upper (short-dash dot) curve: total mass M_p (in $M_\oplus$); solid curve: total core mass $M_{\rm core}$; long-dash dot curve: outer log radius R_p; dashed curve: hydrogen/helium mass in the envelope $M_{\rm env}$; thin vertical solid line: time of onset of migration; thin vertical dash-dot line: time of disk accretion cutoff. The observed mass of Kepler-36 c, with error bars at 84% confidence level, and the observed radius, are given as filled squares.

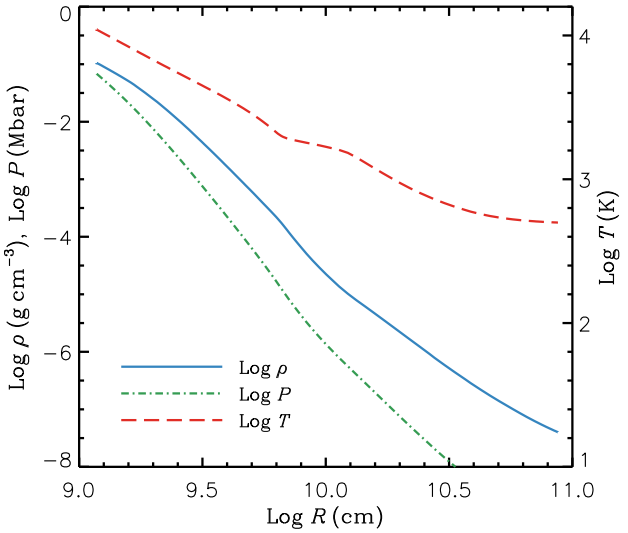

Figure 14. Structure of the H/He envelope of the model in Run 1.00(Old) at time 1.9×10^5 yr, at 1 AU just before the onset of migration. Solid curve (left scale): log density in g cm^{-3}; dash-dot curve (left scale): log pressure in Mbar. The surface value (not plotted) is 7.18×10^{-4} bar. Dashed curve (right scale): log temperature in K. The mean density of the core is 6.13 g cm^{-3}. The change in slope of the temperature curve at log $r = 9.8$ is the boundary between the inner convection zone and the outer radiative zone.

and solids decreases. More H/He mass is accumulated during migration than in the case 1.00(Rev); however the mass loss caused by Roche lobe overflow during the late stages of migration is negligible, only about 0.02 $M_\oplus$ [in Run 1.00(Rev) it was 0.08 $M_\oplus$]. As is the case in the comparison between Run 0.128(Rev) and Run 0.128(Old), the mass of H/He collected during the main gas accretion phase in Run 1.00(Old) is about twice as great as that in Run 1.00(Rev), mainly because of the structure of the hot, low-density outer core in the latter case. Disk cutoff occurs at time 3.3 Myr, with the planet at its present orbital position and with radius 18.7 $R_\oplus$, temperature (at the core boundary) $T_{\rm cb} = 1.04 \times 10^4$ K, pressure $P_{\rm cb} = 0.16$ Mbar, and density $\rho_{\rm cb} = 0.20$ g cm^{-3}. The core and envelope masses are, respectively, 7.32 and 1.40 $M_\oplus$. During migration $M_{\rm core}$ and $M_{\rm env}$ have increased by 0.28 and 0.77 $M_\oplus$, respectively. The outer radiative zone now covers the outer 8% of the mass.

At the beginning of the isolated phase, the intrinsic luminosity is 10^{-8} $L_\odot$ and the cooling time is $\approx 1.0 \times 10^7$ yr. The mass loss efficiency factor is set to 0.18. At an age of 10^8 yr, the temperature $T_{\rm cb}$ has decreased to 5.4×10^3 K and $M_{\rm env}$ to 1.01 $M_\oplus$, a loss of 0.39 $M_\oplus$. The radius has decreased to 5.68 $R_\oplus$ and the luminosity to 10^{-10} $L_\odot$. The outer radiative zone has retreated,

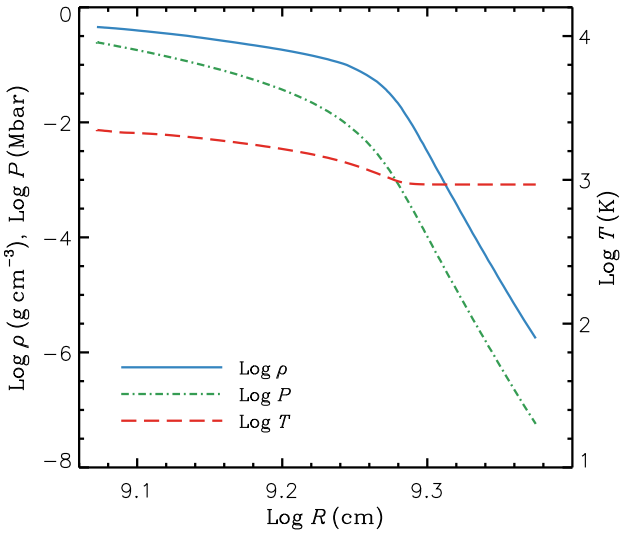

Figure 15. Structure of the H/He envelope of the model in Run 1.00(Old) at time 7.02×10^9 yr (final model). Curves as in Figure 14. The mean density of the core is 6.38 g cm^{-3}.

now covering only 1% of the mass. An additional 0.32

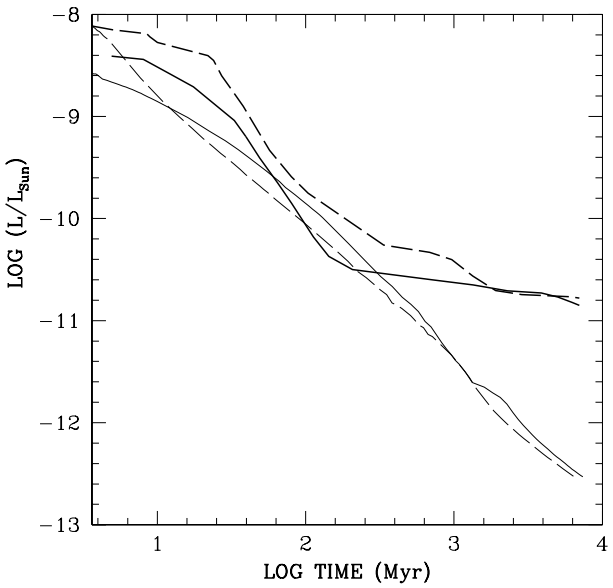

Figure 16. Intrinsic luminosities as a function of time after completion of accretion. Thick solid line: Model 0.128(Rev). Thin solid line: Model 0.128(Old). Thick dashed line: Model 1.00(Rev). Thin dashed line: Model 1.00(Old).

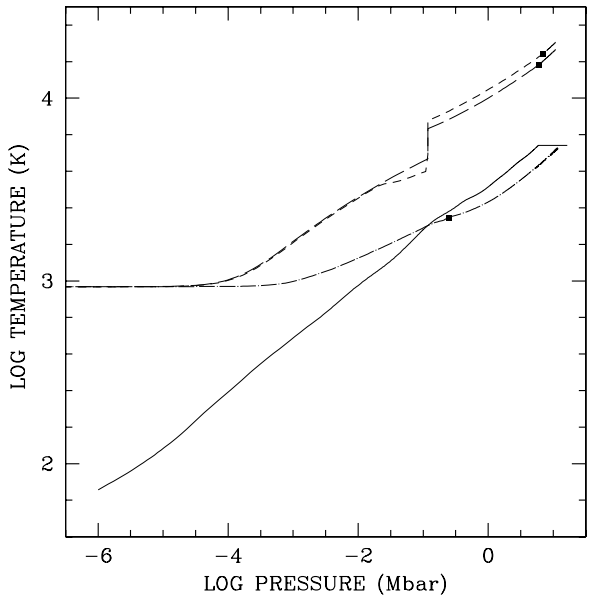

Figure 17. Relation between pressure (in Mbar) and temperature (K) for Kepler-36 c models at time 7 Gyr, including the inner core. Thin solid line: model for the current Neptune from Nettelmann et al. (2013). Note that the assumed composition is different from that in this paper. Short-dashed curve: Run 0.128(Rev). Long-dashed curve: Run 1.00(Rev). Long dash-dot curve: Run 1.00(Old). Solid squares: outer boundary of inner core, or the entire core in the (Old) model. Run 0.128(Old) is not plotted as the curve is practically the same as that for Run 1.00(Old).

$M_\oplus$ is lost up to the end of evolution at 7.02×10^9 yr. The final model (Figure 15) has a radius of 3.72 $R_\oplus$, in good agreement with that of the planet. The mass $M_p = 8.01$ $M_\oplus$, is also in good agreement with that of the observed planet, with $M_{\rm core} = 7.32$ and $M_{\rm env} = 0.69$ $M_\oplus$. The temperature $T_{\rm cb}$ has decreased to 2.22×10^3 K and the intrinsic luminosity to $\log\,(L/L_\odot) = -12.56$ by this time. About half of the envelope mass has been lost through stellar XUV irradiation. The core radius is 1.85 $R_\oplus$ with mean density 6.38 g cm^{-3}. As in the case of Run 0.128(Old), the structure is fully radiative, and envelope masses, temperature $T_{\rm cb}$, and density $\rho_{\rm cb}$ are essentially the same in the two cases.

The intrinsic luminosities as a function of time during the isolation phase for all four of the models presented here are illustrated in Figure 16. Note that the actual luminosities radiated by the planet are many orders of magnitude higher. A comparison of the pressure-temperature relation in the structure of three of the models is shown in Figure 17. The inner core is included, whose structure is calculated assuming an adiabatic temperature gradient. In the cases 0.128(Rev) and 1.00(Rev), the inner-core temperatures are likely above the melting curve of silicates (Millot et al. 2015), so the adiabatic assumption should be fully consistent. In the case 1.00(Old), however, the temperatures are not high enough to satisfy that condition, so the core may be semi-convective, at least in the outer shells. The core calculation for 1.00(Old) was rerun using (the convective-conductive) Equation (29) of D'Angelo & Bodenheimer (2016) rather than (the adiabatic) Equation (30). The result is that the temperature at $r = 0$ is considerably larger (about 10^4 K versus 5.29×10^3 K in the adiabatic case), but the pressure there is only slightly lower (by 0.05 Mbar). There is a negligible difference in the core radius.

4. KEPLER-36 B

We now consider the question of why Kepler-36 b has such different properties (e.g., much higher mean density) from Kepler-36 c, although its orbit, at 0.115 AU, is not far inside that of Kepler-36 c. As mentioned above, Lopez & Fortney (2013) showed, on the basis of in situ post-formation cooling models, that Kepler-36 b could lose its entire H/He envelope as a result of XUV irradiation from the star, while Kepler-36 c would not. The difference is ascribed to the lower $M_{\rm Z}$ of b. Here we confirm that result by providing a formation model for Kepler-36 b. It is assumed to form in situ with an initial core mass of 1.3 $M_\oplus$ and a nebular solid surface density of 1.06×10^4 g cm^{-2}. Otherwise the assumptions and procedure are the same as for Run 0.128(Rev). The

orbital distance and surface density combine to give an isolation mass of 4.3 $M_\oplus$. The corresponding values (Table 1) for Run 0.128(Rev) result in an isolation mass of 7.0 $M_\oplus$, leading to a significantly higher final mass for planet c.

By the time of nebular cutoff at 3.3 Myr, the total mass is 4.48 $M_\oplus$, close to the actual measured mass. The core mass is $M_{\rm icore}$ = 1.3 $M_\oplus$, the heavy-element mass in the envelope is 3.05 $M_\oplus$, and the H/He mass is only 0.13 $M_\oplus$, 3% of the total mass. The quantity ϵ in the expression for XUV mass loss is set to 0.1 and $T_{\rm eq}$ to 978 K. After a total time of 10^7 years, $M_{\rm XY}$ has been reduced to 0.02 $M_\oplus$. The mass loss rate is 3×10^{-9} $M_\oplus$ yr^{-1}, so in another 10^7 yr the entire H/He envelope would be lost. Note that the planet, at the beginning of the isolated phase, has a higher thermal energy and a longer cooling time than would a model planet calculated according to the standard (old) model. Thus, the revised model would have a larger radius than the old during the early part of the cooling phase, and therefore would lose H/He mass more easily, given the same mass loss efficiency parameter. However, if ϵ is reduced, the planet could possibly retain its H/He envelope. A calculation with ϵ = 0.01 shows that the entire envelope would still be lost on a timescale of 2×10^8 yr. If it is further reduced to 0.001, a low-mass H/He envelope ($\approx$ 0.1 $M_\oplus$) is retained for over 10^{10} yr. The borderline value of ϵ, below which some H/He is retained for at least 7 Gyr, is estimated to be 0.002.

After 7 Gyr of cooling, the planet is expected, as observed, to be composed entirely of heavy elements. Once sufficient H/He has been lost and the atmosphere is heavy-element dominated, the energy-limited mass-loss expression (7) is not applicable, as the rate-limiting step for mass loss is the diffusion of H/He out of the atmosphere. But, as the planet loses its envelope, the silicate vapor in the deeper part of the envelope will supersaturate and rain out, so eventually (nearly) all the H/He could be removed. This explanation applies only if the photospheric temperature corresponds to a negligible silicate vapor pressure. Just before the standard calculation would predict that the H/He drops to zero, there will be a phase where diffusion-limited escape may apply, but the amount of gas left at that point is so small that it is not worth considering. If the deeper region is uniform in composition (more precisely, if it has a homogeneous mantle and a well-separated core), then it can cool very efficiently by convection down to a state where it freezes at depth as well as at the surface. The cooling time for this stage to reach something not that different from the standard "cold" picture is only a few hundred million years. If the interior does have a composition gradient, however, the planet could have difficulty cooling and remain in an expanded state.

In this picture, the absence of H/He in Kepler-36 b is associated with the fact that the planet's envelope, composed mainly of silicate vapor, is unable to attract, during the formation phase, enough H/He to survive the XUV irradiation during the isolated phase. Owen & Morton (2016) show that the absence of H/He in the atmosphere of Kepler-36 b can be explained if, at the end of accretion, the heavy-element (core) mass was about 4.4 $M_\oplus$ and the H/He envelope mass fraction was less than 10%. The formation calculations reported here are consistent with their findings. As concluded by Owen & Morton (2016) and by Lopez & Fortney (2013), in the case of the Kepler-36 system, it is clearly the difference in mass between the two planets, rather than the difference in location, that results in the much smaller radius for Kepler-36 b. The higher M_Z of Kepler-36 c allows it to both accrete and retain more H/He than did Kepler-36 b. Figure 18 shows that planets with small radii tend to be of relatively low mass or located close to their star, or both.

The comparison of the Kepler-36 b run and Run 0.128(Rev) for Kepler-36 c shows that the differences in mean density for the two planets can be explained. However, the calculations are based on the assumption that both planets formed in situ at their current orbits. As discussed above, it is also possible that Kepler-36 c formed at a larger distance and migrated inwards to its present orbit; Run 1.00(Rev) also provides a fit to the present properties of the planet. If so, Kepler-36 b could have formed either in situ or farther out in the disk, coupled with migration. In the former case, our calculations still show that the differences between the two planets can be explained. In the latter case, the situation is more complicated, because a detailed calculation has yet to be made. However, as an example, planet b could have formed at 0.75 AU (interior to planet c) with an initial solid surface density of 250 g cm^{-2} (higher than that for planet c), giving an isolation nass of 4.3 $M_\oplus$, close to the measured mass. The shorter formation time during the main solid accretion phase for planet b, along with the higher disk density, would allow it to migrate inward ahead of planet c. Assuming that the amount of H/He gas accreted by planet b up to disk dispersal was comparable to or up to a few times larger than that in the in situ case, then it is still possible that the entire H/He envelope could have been lost by XUV radiation during the isolated phase.

5. SUMMARY AND CONCLUSIONS

We investigate the formation and evolution, up to 7 Gyr, of (sub-Neptune) planets with total mass in the range 4–8 $M_\oplus$. The models are compared with the observed properties of the planet Kepler-36 c, which orbits at 0.128 AU from a star of 1.07 $M_\odot$, and planet Kepler-36 b, with an orbit at 0.115 AU. In the case of Kepler-36 c, we are able to adjust surface density and mass loss efficiency so that models are found that agree quite well with both the mass and radius of the planet at ages consistent with that of the star. In the case of Kepler-36 b, an in situ calculation shows that the entire H/He

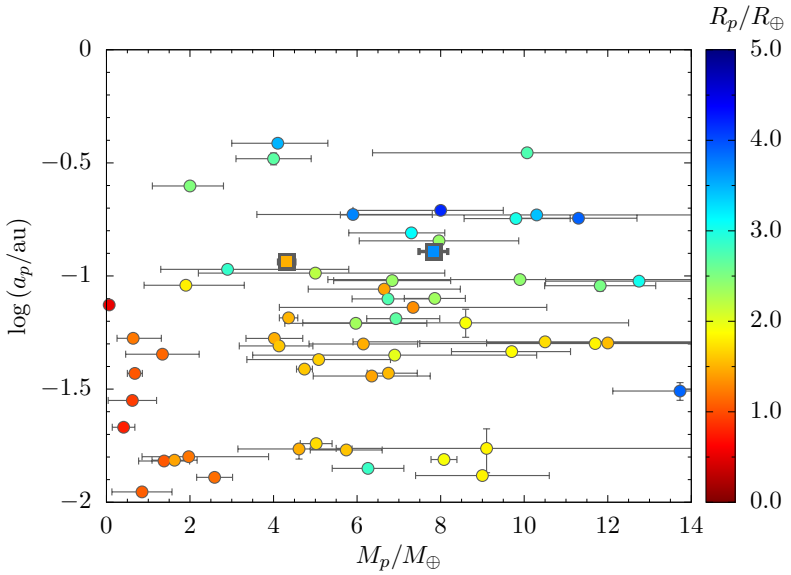

Figure 18. Radius and mass data from Figure 1 are shown with the distance (a_p) of planet from star plotted as a function of mass, with radius indicated by the color scale. The two squares indicate Kepler-36 b (less massive) and c.

envelope is lost, with assumed surface density adjusted to give the planet's observed mass, and with the mass loss efficiency factor set to the standard value of 0.1. Our prescription assumes that the accreting planetesimals are composed of rock, and we take into account the breakup and vaporization of the planetesimals as they interact with the protoplanetary envelope. Dissolved rock vapor rains out to lower levels if the partial pressure exceeds the local vapor pressure. The main result is that the inner core (effectively pure silicate) of the planet remains at relatively low mass but is augmented by an outer core that is also almost pure silicate but arises from compressed silicate vapor that contains only small amounts of H/He and is much hotter than the same region of the planet in the older models. As a consequence, especially during and soon after the accretion stages, it is considerably less dense and causes the planet to have a somewhat larger radius for the silicate-dominated portion alone. This silicate "vapor" (actually a supercritical fluid) is concentrated in a region extending out to as much as several inner core radii, depending on the phase of evolution, and thus dominates the volume and mass of the total (inner plus outer) core.

The generally higher temperatures in the (Rev) models compared with the (Old) models arise in part from the higher total envelope mass in the former case. In the (Old) case much of the accretional energy is radiated away, and the low-mass envelope can store relatively little heat. In the (Rev) models, most of the mass lands in the envelope, and the composition gradient results in limited heat loss by radiation, so this envelope can store more of the accretion energy. Another effect arises from the considerably higher mean molecular weight in the (Rev) case. To maintain comparable pressures in the interiors of the two cases, as required for hydrostatic equilibrium (actually the internal pressures in the (Rev) case are higher than in the (Old) case, at equal total mass), higher temperatures are required in the (Rev) case.

The outer core is bordered by layers in which the mass fraction of rock declines sharply outwards; the composition gradient stabilizes the layers against convection. Thus, it is assumed that no chemical mixing occurs between the inner rock-rich region and the outer region, which is composed basically of H/He. Energy transport through the region with the gradient is by radiation only. The outer layers of H/He amount to only a small fraction of the total mass, but a large fraction of the volume.

The results are compared with models built according to the old prescription, in which all accreted planetesimals end up in the core, and the envelope has a uniform composition of H/He. As in the old models, the revised models have a well-defined core/envelope structure after 7 Gyr, but with different properties. Also considered for both old and revised models for Kepler-36 c, are two different formation scenarios: in the first, the planet forms in situ at 0.128 AU; in the second, the initial phase of rapid solid accretion occurs at 1 AU. Then, during the subsequent phase of slow accretion of gas and solids, the planet migrates inward to its present orbital position. In all cases, during the isolated phase after disk dissipation, mass loss from the H/He envelope is calculated, driven by XUV irradiation from the central star. The main parameters that are varied to provide the fits are the initial solid surface density in the disk at the formation location, and the efficiency factor ϵ in the expression for the XUV mass loss rate. The main conclusion is that our model, which accounts for dissolution of rocky planetesimal material in the envelope of the forming planet, accounts for the properties of the planet Kepler-36 c,

with suitable parameter choices for the initial solid surface density in the disk and for the efficiency factor in the XUV mass-loss formula, with a lower-mass H/He envelope than required by the old models.

A main feature of the revised calculation is the self-consistent treatment of the composition distribution and the equilibrium structure of the envelope of the planet, during its entire formation and evolution. In order to concentrate on the effects of the chemical composition and to allow the calculation of several full formation/evolutionary sequences with a reasonable amount of computer time, a number of simplifications were made, with respect to the state-of-the art simulations of planet formation, e.g., D'Angelo et al. (2014). For example, the additional major refractory heavy-element component, iron, was not included. The dust opacity relies on a fixed opacity table, rather than a detailed simulation of dust settling and coagulation (Movshovitz et al. 2010). The solid accretion rate relies on a simple prescription, rather than the detailed statistical treatment of the evolution and accretion of the planetesimal swarm in D'Angelo et al. (2014). The temperature gradient in the region of variable chemical composition is not well established physically, and it is essentially parameterized. In the high-density inner disk, it is possible that several planetary embryos can form, and later accrete to form one object by giant impacts. The impacts could modify the formation process considerably and could cause mixing between the silicate core and the outer H/He layers. Thus, the details of the numerical results should be viewed with caution. Because of the neglect of Fe, the comparisons with the observed properties of the planet should be given less emphasis than the comparison between the (Rev) models and the (Old) models. The general results of this paper could well stand up, subject to more detailed simulations planned for the future.

The old and revised models, in both the in situ case and in the migration case, form Kepler-36 c with comparable total amounts of heavy elements. In the revised model, at the end of the calculation, as a result of cooling and contraction, the heavy elements are well-concentrated toward the center; the size of that region is only a few percent larger than the size of the core in the old model, with lower mean density by a factor 1.12 [averaging the (1.00) models and the (0.128) models]. The lower mean densities are associated with higher temperatures in the revised models. At earlier times, during the main gas accretion phase before $t = 3.3$ Myr, the density in the silicate-rich outer cores in the revised models is only 3 to 5% as large as in the cores of the old models, the temperature at the base of the H/He-rich region is much higher, and the radius of the outer core is roughly a factor 3 larger than the core radius of the old model at similar times. Thus, less H/He can be accreted in the revised models. The end result is that models of Kepler-36 c according to the revised model have H/He envelopes of 0.29 and 0.37 $M_\oplus$, in models 1.00(Rev) and 0.128(Rev), respectively, only 4 to 5% of the total mass. In contrast, with the old model, the H/He mass is about 0.7 $M_\oplus$, closer to 9% of the total mass, as also found by Lopez & Fortney (2013) and Owen & Morton (2016). At least two factors can account for this difference: (1) the higher temperature and lower density, during gas accretion, in the inner plus outer cores of the revised model compared to those in the core of the old model; and (2) the higher temperature and lower density just outside the outer core in the revised model compared with those just outside the core in the old model. The transition zone, with the composition gradient, plays a less important role, because the zone is relatively thin in both mass and radius during the main gas accretion phase.

It would be difficult observationally to distinguish between the old and revised models, because both have significant amounts of H/He at the photosphere. Also, their radiated luminosities at the present time would be very similar, completely dominated by the stellar input and re-radiation. We speculate that if a mechanism of slow mixing of rock vapor occurs, during the long-term isolation phase, outwards through the composition gradient into the largely convective H/He layers, it might be possible to distinguish between the two models on the basis of observed heavy-element (Z) abundances. The time scale of, for example, double diffusive convection, is quite uncertain (Leconte & Chabrier 2012; Moll et al. 2017), and this or related processes should be considered in future work. The complexities in the theory are reviewed by Garaud (2018). Nevertheless, the mixing of the rock vapor outwards is much more likely during the long-term cooling phase than during the formation (accretion) phase. Note, however, that, first, the condensation of the refractories below the observable photosphere must be taken into account, and, second, the enhancement of Z abundances could also be caused by late accretion of planetesimals. The revised models presented here may also change the speciation of oxygen and carbon in the observable atmosphere, because the high temperature conditions that arise during accretion change the speciation of these elements in the gas phase, as is observed in the models of the deep atmosphere of Jupiter (Fegley & Lodders 1994).

Obtaining the fits to the observed mass and radius of the planet turns out to be very sensitive to the assumed parameters; fine tuning is required. For example, in Run 1.00(Rev) the assumed value of ϵ was 0.04 (note that the generally assumed value is 0.1). The resulting final planet radius R_p was 3.72 $R_\oplus$ with $M_{\rm XY} = 0.29$ $M_\oplus$. If ϵ was taken to be 0.05, $R_p = 3.19$ $R_\oplus$ and $M_{\rm XY} = 0.23$ $M_\oplus$. As another example, in Run 0.128(Rev) the solid surface density was 1.18×10^4 g cm^{-2}; the final mass was 7.80 $M_\oplus$ and the final radius 3.66 $R_\oplus$. A run with the surface density 1.30×10^4 g cm^{-2} gave, at 7 Gyr, a mass of 10.7 $M_\oplus$ and a radius of 5.34 $R_\oplus$, both far too

high to fit the planet. At the beginning of the isolation phase, this run achieved a total mass of 12.6 $M_\oplus$, with $M_{XY} = 3.26$ $M_\oplus$. This model planet is somewhat short of the borderline, above which it would go into rapid gas accretion and become a giant planet. The model fits found here are not necessarily unique; other combinations of parameters could also match the observations. Such a parameter study, which could involve numerous possibilities, is beyond the scope of this paper. As examples, (1) if we allowed planetesimals to migrate relative to the planet, then σ_{init} could be smaller, and (2) if the nebula were to last longer, then mass loss efficiency could be higher.

Numerous discussions of the formation of hot Jupiters or super-Earth/sub-Neptune planets in situ rather than ex situ have appeared in the literature. As summarized by Morbidelli & Raymond (2016), the in situ scenario has two major problems. First, the required solid surface density in the inner disk is very high, in our case around 9 times higher than that in the MMEN (Chiang & Laughlin 2013). Second, in such a massive disk, the protoplanet is expected to migrate inwards, possibly ending up in the star, or at least, inside the boundary of the magnetospheric cavity, on a time scale short compared with the disk lifetime. The first problem could be solved to some extent if it is assumed that the planet did form in situ, but did not accrete from the local disk mass, as was assumed here. Rather, the planet was built from protoplanetary cores (Ward 1997), or planetesimals (Hansen & Murray 2012), or small rock particles (pebbles) (Tan et al. 2016) that migrated inward from the outer regions of the disk and collected at the current orbital position of the planets. These processes would imply more gradual accretion of solids than we have assumed here. In view of these problems, the possibility that the planet formed at a larger distance should also be considered. The actual formation location, taken here to be 1 AU, is arbitrary but is consistent with our assumption that the planetesimals are composed of rock. It is certainly possible that the planet formed farther out, with an ice component. In that case, a much smaller disk surface density would be sufficient to account for the planet's mass. However, if Kepler-36 c formed beyond the ice condensation line, Kepler-36 b might well have also formed in that region, which would require an explanation of how this rocky world lost all of its water in addition to its (much easier to lose) H/He.

Primary funding for the code development for this project was provided by the NASA Emerging Worlds program 15-EW15_2-0007; the specific calculations for the Kepler-36 planets were funded by the NASA Origins of Solar Systems Program grant NNX14AG92G. We are indebted to Ravit Helled, who provided the equation of state tables for compositions that include silicates. We thank Stuart Weidenschilling for informative discussions, and Anthony Dobrovolskis for useful comments on the manuscript. We thank the referee for a careful review which led to improvements in the manuscript. Resources supporting the work presented herein were provided by the NASA High-End Computing (HEC) Program through the NASA Advanced Supercomputing (NAS) Division at Ames Research Center.

REFERENCES

Agol, E., & Fabrycky, D. 2018, in Handbook of Exoplanets, ed. H. J. Deeg & J. A. Belmonte (Berlin: Springer), in press

Alexander, R., Pascucci, I., Andrews, S. et al. 2014, in Protostars and Planets VI, ed. H. Beuther et al. (Tucson, AZ: Univ. of Arizona Press), 475

Alibert, Y., Mordasini, C., Benz, W., & Winisdoerffer, C. 2005, A&A, 434, 343

Bodenheimer, P., Laughlin, G.P., Różyczka, M., & Yorke, H. W. 2007, Numerical Methods in Astrophysics (Boca Raton, FL: Taylor & Francis)

Bodenheimer, P., & Lissauer, J. J. 2014, ApJ, 791, 103

Carter, J. A., Agol, E., Chaplin, W. J. et al. 2012, Science, 337, 556

Chambers, J. 2017, ApJ, 849, 30

Chiang, E., & Laughlin, G. 2013, MNRAS, 431, 3444

D'Angelo, G., & Bodenheimer, P. 2013, ApJ, 778, 77

D'Angelo, G., & Bodenheimer, P. 2016, ApJ, 828, 33

D'Angelo, G., & Lissauer, J. J. 2018, in Handbook of Exoplanets, ed. H. J. Deeg & J. A. Belmonte (Berlin: Springer), doi:10.1007/978-3-319-30648-3-102-1

D'Angelo, G., & Podolak, M. 2015, ApJ, 806, 203

D'Angelo, G., Weidenschilling, S. J., Lissauer, J. J., & Bodenheimer, P. 2014, Icarus, 241, 298

Deck, K. M., Holman, M. J., Agol, E. et al. 2012, ApJ, 755, L21

Erkaev, N. V., Kulikov, Y. N., Lammer, H. et al. 2007, A&A, 472, 329

Fegley, B., Jr., & Lodders, K. 1994, Icarus, 110, 117

Ferguson, J. W., Alexander, D. R., Allard, F. et al. 2005, ApJ, 623, 585

Freedman, R. S., Lustig-Yaeger, J., Fortney, J. J. et al. 2014, ApJS, 214, 25

Freedman, R. S., Marley, M., & Lodders, K. 2008, ApJS, 174, 504

Fulton, B. J., & Petigura, E. A. 2018, arXiv:1805.01453

Garaud, P. 2018, Ann. Rev. Fluid Mech., 50, 275

Ginzburg, S., Schlichting, H. E., & Sari, R. 2016, ApJ, 825, 29
Greenzweig, Y., & Lissauer, J. J. 1992, Icarus, 100, 440
Hansen, B., & Murray, N. 2012, ApJ, 751, 158.
Helled, R., & Stevenson, D. 2017, ApJ, 840, L4
Iglesias, C. A., & Rogers, F. J. 1996, ApJ, 464, 943
Kaltenegger, L. 2017, ARA&A, 55, 433
Kary, D. M., & Lissauer, J. J. 1994, in Numerical Simulations in Astrophysics, ed. J. Franco et al. (Cambridge, UK: Cambridge Univ. Press), 364
Kippenhahn, R., & Weigert, A. 1990, Stellar Structure and Evolution (Berlin: Springer)
Leconte, J., & Chabrier, G. 2012, A&A, 540, A20
Lissauer, J. J. 1987, Icarus, 69, 249
Lissauer, J. J., Dawson, R. I., & Tremaine, S. 2014, Nature, 513, 336
Lissauer, J. J., Hubickyj, O., D'Angelo, G., & Bodenheimer, P. 2009, Icarus, 199, 338
Lissauer, J. J., Jontof-Hutter, D., Rowe, J. F. et al. 2013, ApJ, 770, 131
Lopez, E., & Fortney, J. J. 2013, ApJ, 776, 2
Lopez, E., Fortney, J. J., & Miller, N. 2012, ApJ, 761, 59
Lozovsky, M., Helled, R., Rosenberg, E. D., & Bodenheimer, P. 2017, ApJ, 836, 227
Lyon, S. P., & Johnson, J. D. 1992, Report LA-UR-92-3407, SESAME: The Los Alamos National Laboratory Equation of State Database, Los Alamos, NM
Marcy, G., Isaacson, H., Howard, A. W. et al. 2014, ApJS, 210, 20
Melosh, H. J. 2007, Meteoritics & Planetary Science, 42, 2079
Millot, M., Dubrovinskaia, N., Černok, A. et al. 2015, Science, 347, 418
Moll, R., Garaud, P., Mankovich, C., & Fortney, J. J. 2017, ApJ, 849, 24
Morbidelli, A., & Raymond, S. N. 2016, JGR Planets, 121, 1962
More, R. M., Warren, K. H., Young, D. A., & Zimmerman, G. B. 1988, Phys. Fluids, 31, 3059
Movshovitz, N., Bodenheimer, P., Podolak, M., & Lissauer, J. J. 2010, Icarus, 209, 616
Murray-Clay, R. A., Chiang, E. I., & Murray, N. 2009, ApJ, 693, 23
Nettelmann, N., Helled, R., Fortney, J. J., & Redmer, R. 2013, Planet. Space Sci., 77, 143
Owen, J. E., & Morton, T. D. 2016, ApJ, 819, L10
Owen, J. E, & Wu, Y. 2016, ApJ, 817, 107
Podolak, M., Pollack, J. B., & Reynolds, R. T. 1988, Icarus, 73, 163
Pollack, J. B., Hubickyj, O., Bodenheimer, P. et al. 1996, Icarus, 124, 62
Ribas, I., Guinan, E. F., Güdel, M., & Audard, M. 2005, ApJ, 622, 680
Rogers, L. A. 2015, ApJ, 801, 41
Rogers, L. A., Bodenheimer, P., Lissauer, J. J., & Seager, S. 2011, ApJ, 738, 59
Safronov, V. S. 1969, Evolution of the Protoplanetary Cloud and Formation of the Earth and Planets (Moscow: Nauka)
Saumon, D., Chabrier, G., & van Horn, H. M. 1995, ApJS, 99, 713
Seaton, M. J., Yan, Y., Mihalas, D., & Pradhan, A. K. 1994, MNRAS, 266, 805
Stevenson, D. J. 1984, Lunar Planet. Sci. XV, 822
Tan, J. C., Chatterjee, S., Hu, X., Zhu, Z., & Mohanty, S. 2016, Proceedings of the IAU, 29A, 6
Thompson, S. L., & Lauson, H. S. 1972, Technical Report SC-RR-61 0714, Improvements in the Chart D Radiation-Hydrodynamics Code III: Revised Analytic Equation of State, Sandia National Laboratories, Albuquerque, NM
Van Eylen, V., Agentoft, C., Lundkvist, M. S. et al. 2018, MNRAS, 479, 4786
Vazan, A., Kovetz, A., Podolak, M., & Helled, R. 2013, MNRAS, 434, 3283
Venturini, J., Alibert, Y., & Benz, W. 2016, A&A, 596, 90
Venturini, J., & Helled, R. 2017, ApJ, 848, 95
Ward, W. R. 1997, ApJ, 482, L211
Watson, A. J., Donahue, T. M., & Walker, J. C. 1981, Icarus, 48, 150
Winn, J. N., & Fabrycky, D. C. 2015, ARA&A, 53, 409